Wave-driven current and vortex patterns at an open beach: Insights from phase-resolving numerical computations and Lagrangian measurements

Andreas Bondehagen, Volker Roeber, Henrik Kalisch, Marc P Buckley, Michael Streßer, Marius Cysewski, Jochen Horstmann, Maria Bjørnestad, Olufemi E Ige, Hege G Frøysa, et al.

Coastal Engineering 193 (2024) 104591

Contents lists available at ScienceDirect

Coastal Engineering

journal homepage: www.elsevier.com/locate/coastaleng

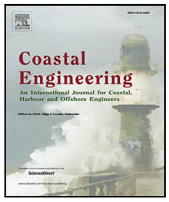

Wave-driven current and vortex patterns at an open beach: Insights from phase-resolving numerical computations and Lagrangian measurements

Andreas Bondehagen [a], Volker Roeber [b,c], Henrik Kalisch [a,*], Marc P. Buckley [d], Michael Streßer [d], Marius Cysewski [d], Jochen Horstmann [d], Maria Bjørnestad [e], Olufemi E. Ige [a], Hege G. Frøysa [f], Ruben Carrasco-Alvarez [d]

[a] University of Bergen, PO Box 7800, Bergen, 5020, Norway
[b] Université de Pau et des Pays de l'Adour, E2S-UPPA, SIAME, Anglet, 64600, France
[c] Department of Oceanography, University of Hawai'i at Manoa, Honolulu, 96822, USA
[d] Helmholtz-Zentrum Hereon, Geesthacht, 21502, Germany
[e] The Norwegian Meteorological Institute, Allégaten 70, Bergen, 5007, Norway
[f] Aqua Kompetanse AS, Havbruksparken, Storlavika 7, Flatanger, 7770, Norway

ARTICLE INFO

Dataset link: http://dx.doi.org/10.5281/zenodo.7843727

Keywords:
Surf zone circulation
Boussinesq model
Rankine vortex
Surface drifters

ABSTRACT

Wave-driven currents have a substantial impact on local circulation patterns in and across the surf zone, and are responsible for cross-shore and longshore exchange of mass and momentum over a broad range of spatial and temporal scales. Nearshore currents may drive sediment transport, lead to beach erosion, and also affect the spread of bacteria and other marine microorganisms, as well as the distribution of pollutants such as chemicals and microplastics. In addition, surf zone currents can cause hazardous conditions for beach-goers in the form of rip currents.

It is known from previous work (Chen et al., 2003; Feddersen et al., 2011; Hally-Rosendahl and Feddersen, 2016) that Boussinesq-type models in combination with appropriate boundary conditions and wave breaking capabilities can function as powerful tools for the analysis of circulation patterns in the surf zone. In the present work, data from a recent field campaign reported on in Bjørnestad et al. (2021) are used to further validate the capability of Boussinesq systems to simulate nearshore dynamics.

The numerical model is then used to study the influence of tidal elevation, peak direction and directional spread of the incoming wavefield on the quantity, extent, and circulatory magnitude of the nearshore circulation. In addition, fundamental features such as horizontal eddies are investigated, and comparisons are made to solid-body rotation and irrotational vortices.

Overall, it is observed that local variations in the bathymetry across the surf zone are the controlling factor regarding the size of these circulations, and an increasing tidal level, which can be seen as a uniform offset to the bathymetry, favors the generation of larger vortex patterns. For a given tidal stage, the directional spread of the incoming wavefield has the most pronounced influence on the size and strength of the nearshore eddies while the peak direction has the strongest effect on the total number of circulations.

1. Introduction

The nearshore zone is a dynamic environment where waves interact with the sea bed and coastal structures to create complex and diverse hydrodynamics. One prominent wave-induced effect is the nearshore circulation, which may consist of longshore currents, rip currents and circulation cells (Putrevu and Svendsen, 1999; Svendsen, 2006; Castelle et al., 2016). Understanding the physical processes that govern nearshore circulation is important for a variety of applications, such as coastal engineering, beach management, and wave energy extraction (Inman and Brush, 1973; Roberts et al., 2014; Nader et al., 2017; Davidson-Arnott et al., 2019). Nearshore currents transport sediment, nutrients and pathogens along the coast and between the surf zone and the inner shelf, and have a major effect on the local ecology, beach erosion and general coastal morphology (Rilov et al., 2008; Shanks et al., 2010; Feddersen, 2014; Brown et al., 2015), as well as issues of recent interest, such as distribution of microplastics (Larsen et al., 2023).

In recent years, numerical models have become an essential tool for studying nearshore hydrodynamics, and have also been used to study longshore currents, rip currents and more general surfzone dynamics

* Corresponding author.
E-mail address: henrik.kalisch@uib.no (H. Kalisch).

https://doi.org/10.1016/j.coastaleng.2024.104591
Received 26 May 2023; Received in revised form 8 May 2024; Accepted 30 July 2024
Available online 3 August 2024

(Chen et al., 2003; Long and Özkan-Haller, 2005; Feddersen et al., 2011; Clark et al., 2011). In particular phase-resolving (Boussinesq-type) wave models have been shown to accurately reproduce complex wave behavior in the nearshore (see Lynett et al. (2017) and references therein for an overview).

Several works have investigated the ability of Boussinesq-type systems to model various features of wave-induced nearshore currents. Feddersen et al. (2011) and Clark et al. (2011) used the Boussinesq model *funwaveC* based on the original Nwogu system with and without coupling to an advection model to simulate tracer concentration observed in a dye release experiment at Huntington Beach in California, and obtained found good agreement when considering low-frequency eddy motion, cross-shore diffusivity, and longshore variability of the tracer plume. In Feddersen (2014), it was shown that Boussinesq models are able to simulate salient features of the surfzone circulation, and the creation of surfzone eddies was investigated. In Hally-Rosendahl and Feddersen (2016), it was shown that the *funwaveC* model is able to generate surfzone eddies and transient rip currents which were exhibited by dye release experiments detailed in Hally-Rosendahl et al. (2015). Addressing the issue with traditional Boussinesq models which are not able to resolve the vertical structure of the flow (Hally-Rosendahl and Feddersen, 2016), more recent work by Baker et al. (2021) focussed on the influence of the bathymetry on the nature of eddy motion and three-dimensional effects.

In the present work, we use the phase-resolving nearshore Boussinesq Ocean and Surf Zone model (BOSZ) introduced in Roeber et al. (2010) and Roeber and Cheung (2012b), to investigate the properties of surf zone circulation patterns. Intensive benchmarking was conducted in Roeber and Cheung (2012a) and Lynett et al. (2017). Other studies using BOSZ include tsunamis, long and storm waves (Horrillo et al., 2015; Morichon et al., 2021; Li et al., 2014), nearshore wave transformations (Li et al., 2014; Filipot et al., 2019; Varing et al., 2020, 2021; David et al., 2021), wave run-up (Roeber and Bricker, 2015; Pinault et al., 2020; Kalisch et al., 2024), and transport processes (Watanabe et al., 2021).

In the present work, particular attention is paid to the influence of tidal elevation, peak direction, and directional spread of the incoming wavefield on the nature, extent, and circulatory magnitude of the nearshore circulation. Our study complements previous works focusing on the importance of the directional spread of the incoming wave field on the nature of the developing nearshore currents such as the observational study (Spydell et al., 2009), and numerical studies such as Spydell and Feddersen (2009) and Choi et al. (2015) and also Suanda and Feddersen (2015) where it was shown that for normally-incident waves, rip current driven exchange velocities depend strongly on the wave directional spread. More recent contributions in the same direction include (Baker et al., 2021), focussed on the influence of the bathymetry on the nature of eddy motion and O'Dea et al. (2021) who found that directional spread is a major factor influencing the enstrophy and the spectral energy of surf zone vorticity.

Many studies focussing on the validation of numerical methods for the simulation of nearshore circulation patterns have focussed on comparison with dye experiments (Feddersen et al., 2011; Clark et al., 2011; Grimes et al., 2021), but other works have addressed comparison with drifter observations (Spydell and Feddersen, 2009), or comparison with Eulerian measurements (Feddersen, 2014; Baker et al., 2021). To validate the velocity predictions provided by the BOSZ model, we compare the simulation results to data from a recent measurement campaign conducted at a beach on the island of Sylt, located off the German North Sea Coast near the border with Denmark. In this campaign, oranges were used as surface drifters in connection with a two-camera stereo imaging system as explained in Bjørnestad et al. (2021). Here we analyze the tracks of the orange drifter computed from the captured frames, and compare with simulated drifter motions based on Boussinesq simulations. By replicating the drifter movement using the Boussinesq model, the accuracy of the model in capturing the essential features of the nearshore velocity fields can be assessed. Indeed, while somewhat limited by the size of the field of view (FOV), it is shown in Section 3 that the comparison of the measured orange drifter positions and numerical drifter positions the comparison is favorable. More extensive drifter campaigns were conducted among others by Spydell et al. (2007) and Scott et al. (2014) who gave a very comprehensive picture of possible scenarios for nearshore currents based on tidal level. In particular, Scott et al. (2014) defined three distinct behavioral groups which can be classified roughly as *entrance and exit*, *rotation and longshore* and pure *longshore*. As will be shown in the body of this paper, all three possibilities can be realized with the numerical Boussinesq model used here (see Fig. 1).

The main goal of this study is then to understand the influence of the peak direction D_P of the incoming wave field, the directional spread σ_θ of the applied spectrum and the tidal level on the nature of nearshore circulation patterns prevalent for locations similar to the experimental site. Due to prevailing conditions at sites of interest, most field studies are limited to varying one or two of these parameters and may not be able to paint a complete picture of possible scenarios. In contrast, since we are able to set the parameters numerically, in the present work we can investigate the combined influence of these three quantities. In particular, we quantify the preponderance, strength, and size of the developing eddies, and the statistics of their joint dependence on the above parameters, eliminating the potential for false positives. As a tool to assess the strength and size of the horizontal eddies featuring in the nearshore, we use the Rankine vortex as a proxy for the eddy motion. In fact, while some of the largest eddies, and those located in very shallow water are highly eccentric, about 90% of the detected eddies are approximately circular. Since Rankine vortices, consisting of a solid-body rotation near the center and an irrotational flow further out can be easily quantified by the size and circulation strength, these vortices serve as a convenient tool to quantify the horizontal eddies observed.

The overall plan of the paper is as follows. The field experiments are described in Section 2, and comparison between field data and numerical simulations are shown in Section 3. The dependence of the nearshore circulation patterns on the applied parameters are investigated at length in Section 4. Finally, the results are discussed in Section 5.

2. Field measurements

In order to create a baseline for the numerical study of the surf zone circulation, a measurement campaign was conducted at a beach on the island of Sylt, located just off the German Coast. Wave poles with graduation, pressure sensors and an Acoustic Doppler Velocimeter (ADV) were deployed at low tide, and oranges were introduced by a swimmer. The oranges acted as surface drifters, and a custom-built two-camera stereo imaging system was used to track the oranges. According to data from Sharifi et al. (2007), the density of a typical orange is only slightly lower than seawater, and should be about 97% submerged. Nevertheless, the oranges were clearly visible in the camera images, and it was possible to pinpoint them with sufficient accuracy.

The measurement campaign was designed with the main goal of understanding wave-by-wave properties in the surf zone with respect to particle motion in non-breaking waves (see Bjørnestad et al. (2021)). The study of surf zone dynamics was a secondary goal in the campaign and some compromises especially regarding the field of view of the cameras compared to the size of circulation cells. Nevertheless, it appears that the present study is one of the first to report on surf zone dynamics using small drifters tracked with stereo imagery.

2.1. Stereo imaging system

The two-camera imaging system used to track the drifters was specifically developed for this study. Two Canon 5MP, global shutter CMOS digital cameras (Victorem 51B163-CX, IO Industries) were each

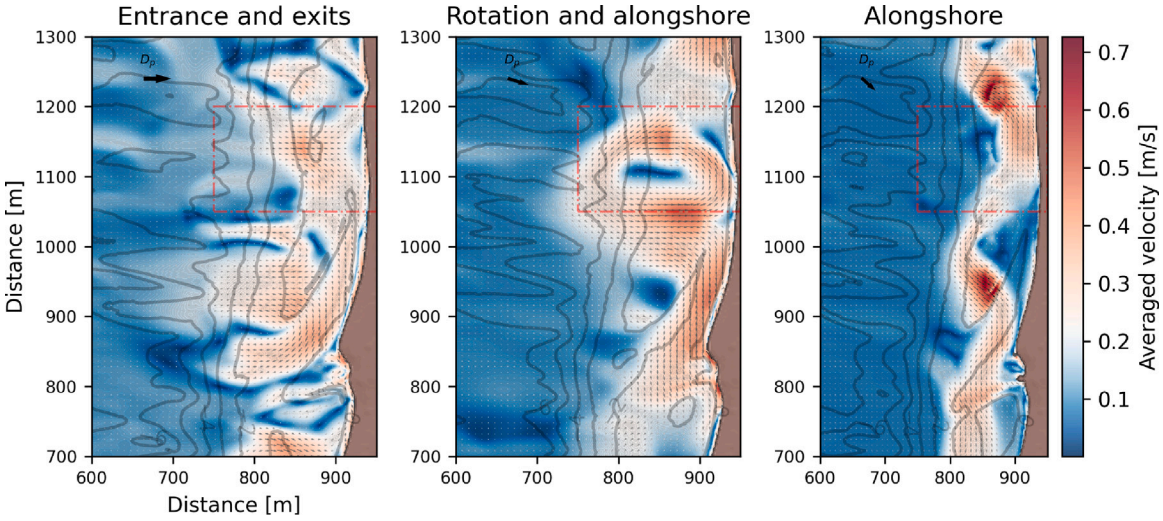

Fig. 1. Examples of the three types of large scale Lagrangian behavior from the same location for different model inputs. Left panel: Fluid enters and leaves the surf zone, rip currents are likely (tidal level: 0, $\sigma_\theta = 20°$, $D_P = 0°$). Middle panel: A large eddy is seen in the upper part of the image. It is fed mass from the longshore current from the north, and feeds into the longshore current to the south. Both longshore currents are north to south (tidal level: 0.5 m, $\sigma_\theta = 0°$, $D_P = 20°$). Right panel: An overall north to south longshore flow is present. No eddies are visible (tidal level: −0.25 m, $\sigma_\theta = 0°$, $D_P = 40°$). The dashed–dotted line shows the field of view (FOV) of the stereo imaging system. The bathymethry is contoured for every meter.

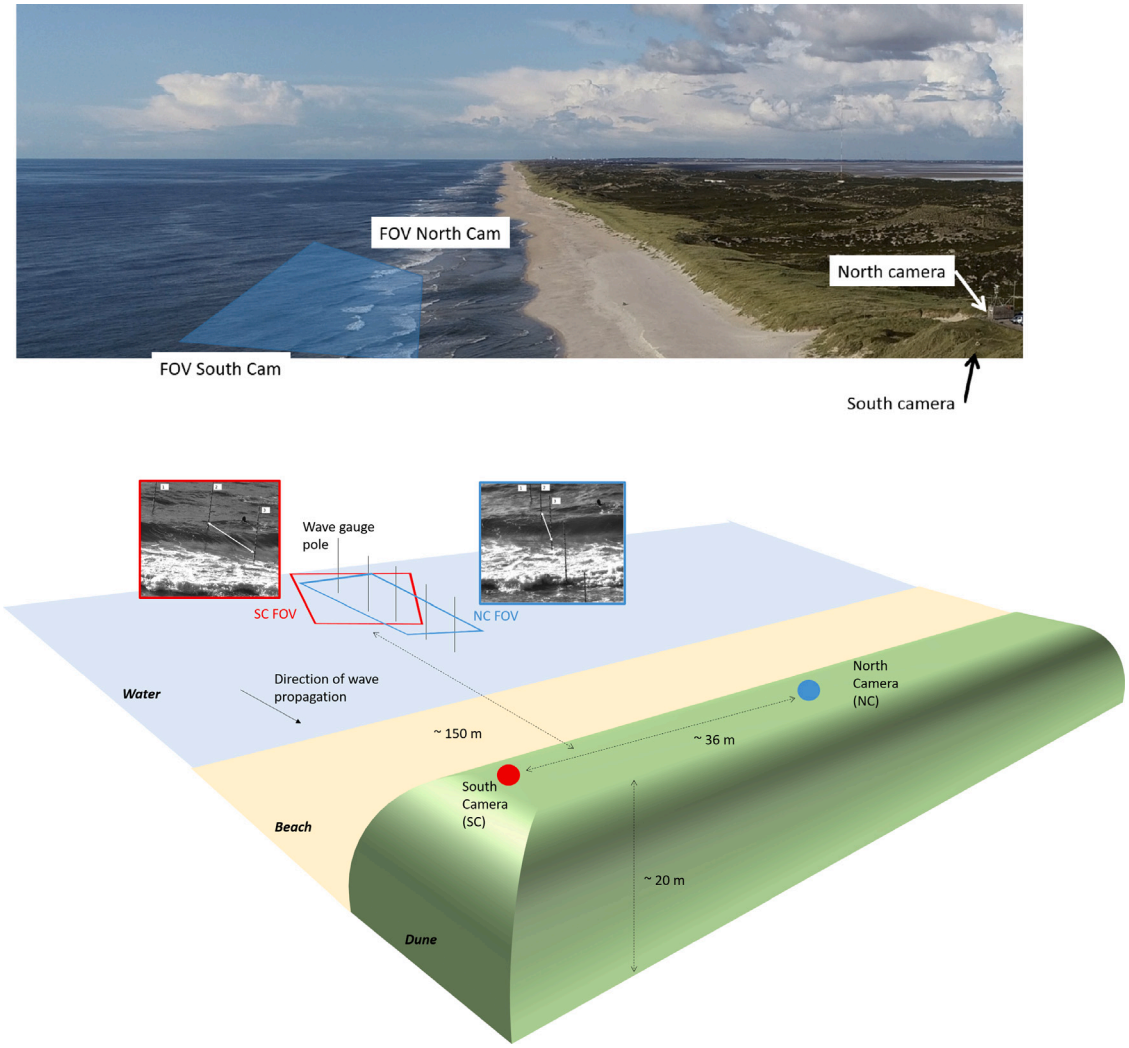

Fig. 2. Upper panel: Photograph taken by a drone overlooking the experimental site. Lower panel: Experimental set-up. Wave poles were lined up in the direction of the incoming wavefield. Two cameras (North cam and South cam) were mounted on solid foundations atop dunes overlooking the beach. The two fields of view overlapped in a region including the first three wave poles. Pressure sensors were mounted near the base of each pole. An ADV was mounted at the sea bed near Pole 2.

fitted with an EF 50 mm f/2.8L lens. The cameras were placed on a ridge overlooking the beach at the Bunker Hill site, at a distance of 35 m from one each other. The cameras were focused on a particular location within the surf zone at a distance of approximately 150 m from each camera. The cameras were synchronized by a computer-controlled function generator (National Instruments PCIe 6612). A sketch of the instrumental setup is show in Fig. 2. Stereo imaging of the sea surface in order to describe the wave motion has been used by a number of authors (see for example Benetazzo (2006), Gallego et al. (2008), de Vries et al. (2011) and Bergamasco et al. (2017)). In the present case, the cameras are used only for tracking the surface drifters which simplifies the data analysis considerably. Six graduated aluminum poles were jetted into the sand of an intertidal sandbar at low tide. The array of poles was aligned so as to be approximately perpendicular to the crests of incoming waves. The most seaward pole (Pole 1) was about 80 m from the shore, and the closest pole (Pole 6) was about 20 m from the shoreline. Since the graduated poles were within the field of view of the stereo cameras (acquiring at 30 frames/s), these could also used as optical wave gauges.

2.2. Experimental procedure and data analysis

Oranges were deployed manually near Pole 1. Images were acquired at 30 frames/second from both cameras. The data used in this article were acquired between 10:30 and 11:00 UTC on the 8th of September, 2019. At this time, the sea state was characterized by a buoy in depth of 10 m and 1 km offshore as 0.75 m significant waveheight H_s and peak period of 9.1 s. The incoming wavefield was slightly skewed from the vantage point of the beach, and the spectrum appeared to be fairly broad. The mean wind speed was approximately 5 m/s from NNW.

In order to obtain the intrinsic and extrinsic parameters for the two 50 mm cameras, a stereo camera calibration was conducted with the Matlab toolbox Stereo Camera Calibrator. Pairs of individual frames from camera footage were examined visually, and orange positions were pinpointed and recorded. Using the calibration parameters, a triangulation of the stored pixel positions was then performed to construct 3D world-coordinate points of the drifter positions. In order to create an appropriate coordinate system, a reasonable assumption is to assume that the crests are perpendicular to the line of poles such as indicated in Fig. 2. A horizontal vector was found by using two known GPS-positions at Pole 2 and Pole 3, and with this a vertical vector along Pole 2 was found. With the described vectors, a 3D coordinate system can be created where the origin is placed at the bottom of Pole 2, the x-axis is pointing along the poles towards the beach, the y-axis is pointing along the wave crests and the z-axis is pointing upwards. With the three orthogonal basis vectors, the orange positions are placed in the described coordinate system and then projected onto the xy-plane.

3. Comparison with Boussinesq model

The main grid used in this study is the bathymetry provided by the LiDAR scan conducted by the LKN (2021). This dataset was originally scanned by drone with a resolution of 10 by 10 cm covering the entire coast of Sylt in June 2020. The LiDAR data was only collected to about 600 m off the coast. This was not far enough offshore since the Bunker Hill buoy where wave conditions are measured is located further at about 1 km offshore. Hence it was necessary to merge the bathymetry data supplied by LKN with EMODnet data (emodnet, 2020). These data are given on a coarse grid with a resolution of about 115 m by 115 m. This dataset is used wherever the LiDAR data is not measured, which is farthest offshore at depths lower than 6 m. For all practical purposes this dataset encompasses only small parts of the domain, as all depths deeper than the buoy location are set to the buoys depth. To fit these two datasets together they were interpolated to a grid size of 2 m by 2 m, which also defines a mesh which is practically possible to simulate on. After doing this for the entire site of Sylt, it is only a matter of choosing a subset of the entire domain to simulate. The bathymetry used in the computations shown in the left panel of Fig. 4. The subdomain used to compare the oranges are 1000 m by 1000 m, stretching approximately 900 m offshore. The maximum depth is set to the depth at the location of the buoy outside our location.

Since the bathymetry provided by the LKN was collected several months after the field campaign, there are some differences with the bathymetry on the days of the campaign. In order to gain more confidence in the ability of the Boussinesq system to simulate the drifter positions, a second bathymetry (from 2016) was used to do the comparison as well. A transect of both bathymetries as well as the measured bathymetry from the week of the campaign are shown in the supplementary material.

The wave data gathered by the Bunker Hill buoy outside Sylt contains various parameters regarding the wavefield for every half hour throughout the 7th to 8th of September 2019. The data includes the spectral power density function $E(f_i)$ given at discrete frequencies as well as some directional information which allows reconstruction of a two-dimensional spectrum (see Appendix A). An example of a one-directional and reconstructed two-dimensional spectrum is shown in the right panel of Fig. 4. Comparisons between orange drifter tracks and numerical drifter paths are shown in Fig. 5. Comparisons for the 2016 bathymetry can be found in the supplementary material. For these simulations, we assume that the cross-shore direction is the longitude and the longshore direction is the latitude, which is approximately valid at this location on Sylt. The origin is chosen in the lower left corner of the computational domain.

The BOSZ model is used to compute the nearshore wave and velocity field for the Sylt bathymetry, driven by a particular offshore wave state, and a given tidal level. These runs are done for 1 hour each, assuming that the three main parameters are constant throughout. The velocity field furnished by a run with the BOSZ model can be used to track fluid particles. Indeed, it has been shown that long-wave models such as the KdV equation are capable of describing wave-by-wave dynamics of particle tracers rather accurately (Borluk and Kalisch, 2012; Bjørnestad et al., 2021). Velocity fields are extracted at each time step, and the drifters are tracked using the following differential equations for inertial particles:

$$\begin{aligned}
\frac{dX}{dt} &= U, \\
\frac{dY}{dt} &= V, \\
\frac{dU}{dt} &= \frac{u-U}{\tau} + \beta\frac{du}{dt}, \\
\frac{dV}{dt} &= \frac{v-V}{\tau} + \beta\frac{dv}{dt},
\end{aligned}$$

where X and Y are the horizontal coordinates of the drifter, $\tau = \frac{a^2}{3\beta\nu}$ is called *Stokes* response time, a is the particle radius, ν is the kinematic viscosity, $\beta = \frac{3\rho_f}{\rho_f+2\rho_p}$ is connected to the added mass of the drifter, ρ_f is the fluid density and ρ_p is the particle density (see Bakhoday-Paskyabi (2015) and Santamaria et al. (2013) for example). In particular, note that in general there is a difference between the drifter velocity given by U and V and the fluid velocity given by u and v. At this point, tidal currents could also be introduced into the differential equations governing the drifter motion. However, since measured tidal currents were extremely weak during the campaign, this option is not pursued further.

For the comparison between measured and computed paths, we use the stereo reconstruction of the orange path to create the initial position and velocity of the numerical drifters. Around the given initial position, we place 100 drifters randomly in a circle of radius 20cm to compensate for errors in the location of the oranges. We also add a random component to the measured velocities of the oranges from the pictures which measures ±50%. After a 500 second start-up period, the wavefield is developed in the sense that the total energy and enstrophy

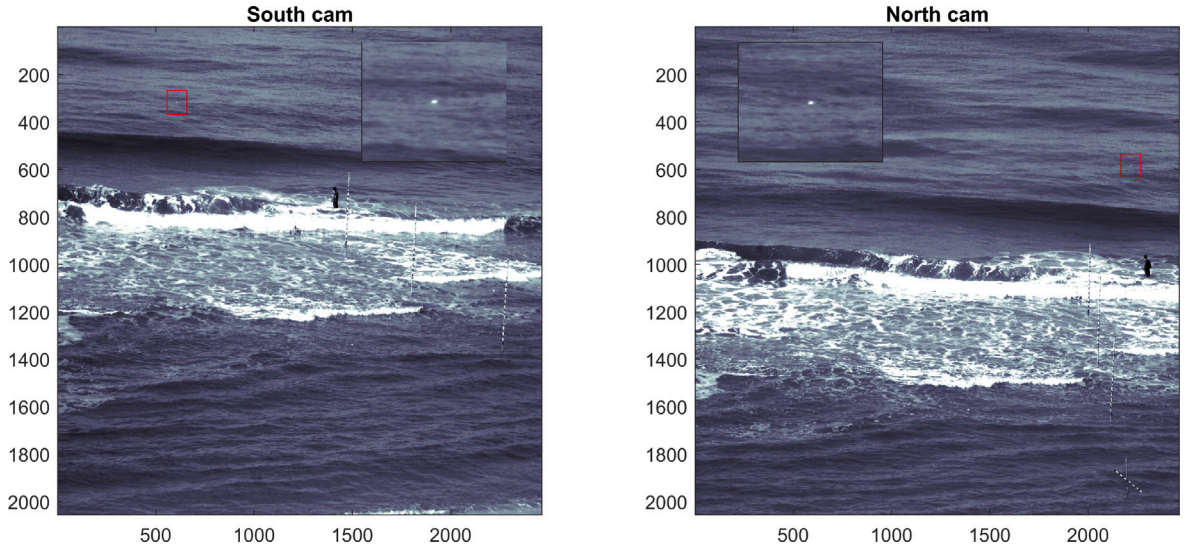

Fig. 3. Raw image of South Cam and North Cam with overlapping FOV. Axes are in pixel coordinates. An orange drifter is located in the area indicated with a red square. The small inset shows a zoomed-in view of the red box, and the orange is clearly visible in both images. As the orange moves, pixel coordinates are recorded for South Cam and North Cam in each frame. The pixel coordinates are then triangulated to find the position of the drifter in a chosen reference frame.

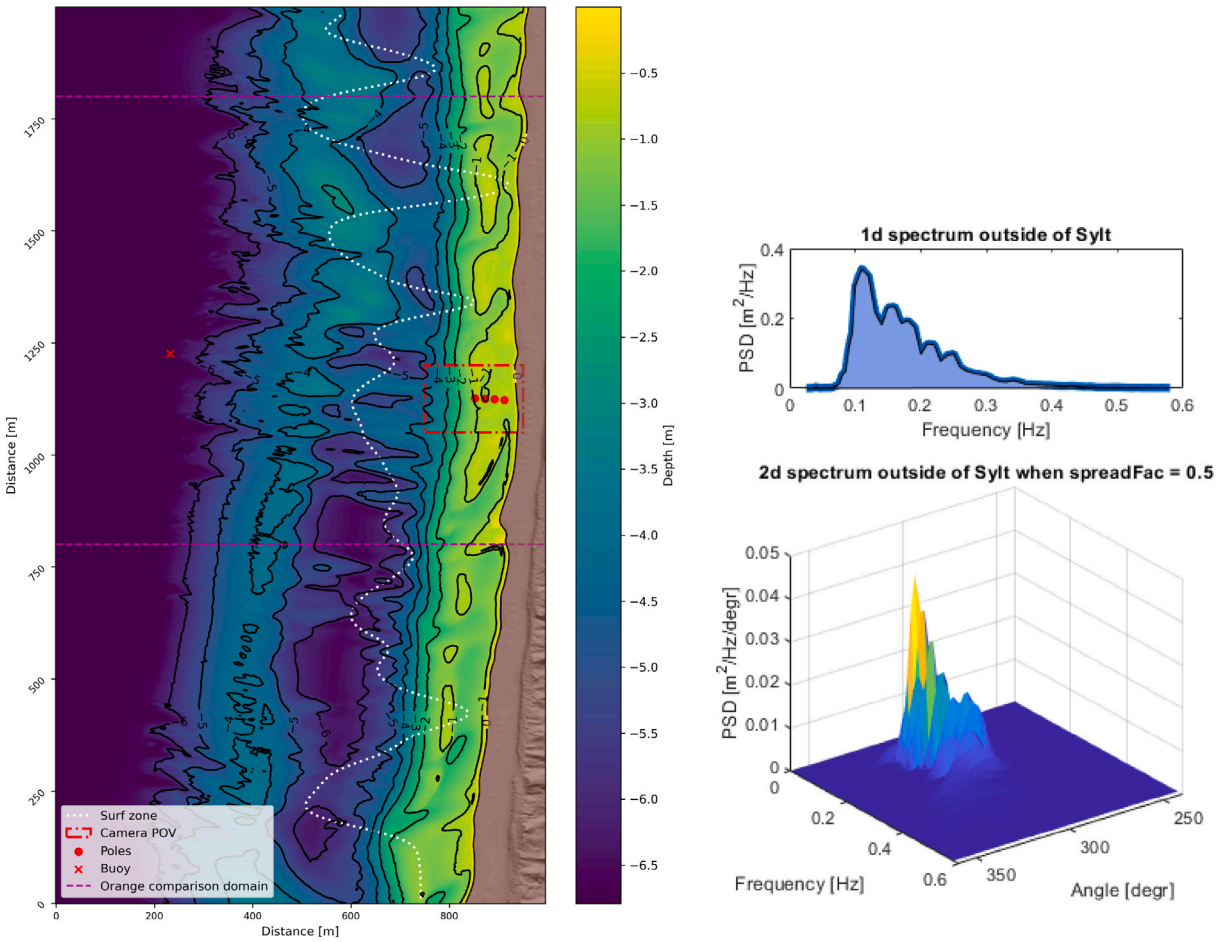

Fig. 4. Left panel: The bathymetry around the experimental site on Sylt in June 2020. The rectangle and dots represent the field of view of the cameras and the visible poles as seen in Fig. 3. The red cross shows where the buoy outside of Bunker Hill is located. The pink dashed line denotes the smaller domain used in the comparison section, while the entire domain is used during the circulation analysis. The white dotted line shows the approximate start of the surf-zone. Right panel: On top is the raw recorded data of $E(f_i)$ supplied by the buoy, and below the estimated data $E(f_i, \theta_j)$ with a cosine squared assumption and $\sigma_\theta = 20°$.

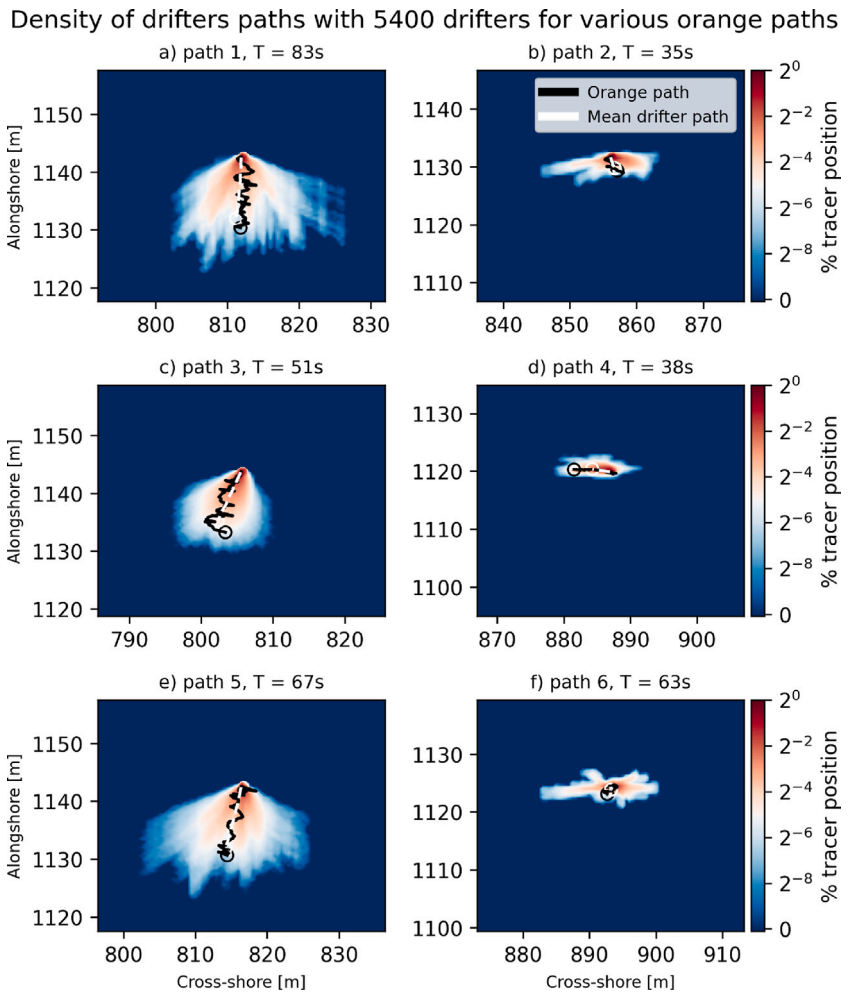

Fig. 5. Results from the drifter simulations for the June 2020 bathymetry. For each drifter path, a 40 m by 40 m area is plotted where every 0.5 m by 0.5 m grid cell counts how many numerical drifter have passed through that particular cell have passed after the T seconds after the orange was released. This number divided by the total number of drifter yields the plotted values. The drifters in (a), (c) and (e) were tracked outside the sandbar and show large movements, while (b), (d), and (f) are in the inner surf zone between the sandbar and the beach, and exhibit smaller movements.

oscillates around a mean (see supplementary material). When the 500 s start-up period has passed the drifters are added to the simulation. Each drifter is simulated independently before being averaged in an ensemble.

After simulating the numerical drifters the positions are stored in a seven-dimensional array with entries for tide level, directional spread σ_θ, random wave phase seed ψ_0, orange path number, numerical drifter number, time stamp, X-coordinate or Y-coordinate. For plotting the data it was necessary to reduce the dimensions to maximum three. This was done by creating a new X and Y grid where for every drifter we create a binary map where 1 means that the drifter was in this location for any given timestep. This creates the slightly different seven-dimensional array with the following dimensions: tide level, σ_θ, ψ_0, orange path number, drifter number, X-index and Y-index. To reduce the system and find the percentage of drifters going through any particular location is then a matter of summing the tensor and dividing by the total number of instances summed together. In Fig. 5 this is shown for tide level, spread, seed, and drifter number summed together, such that the independent variables left to be evaluated are the orange path number, X-index and Y-index. Lastly the average position of the drifters for each orange path is calculated. Thus the color in the mapping can be interpreted as what percentage of drifters at some time reached that cell.

Note that there is a sandbar located at a cross-shore distance of about 830 m to 850 m from the origin of the numerical domain. This sandbar is where waves primarily break, and the drifters tracked in Fig. 5 can be classed in whether they are offshore of the sandbar or not. Path 1, 3, and 5 are located outside of the bar, and are hence moving through larger waves, but also have higher initial velocities. Path 2, 4, and 6 on the other hand are located between the sandbar and the beach, and move at a much slower pace. While individual drifter simulations may not always match the experimentally determined drifter positions, the average values of the numerical drifters show good resemblance to the oranges' actual end position.

The spreading of drifter location also makes sense. For oranges with larger movement, there is a larger spreading of the computed drifter locations, perhaps exaggerated slightly by the initial velocity variation in the simulation model, but also due to the fact that the drifters exhibit a chaotic system (Brown and Smith, 1991). In summary, the Boussinesq model is able to reproduce the experimental drifter paths with reasonable accuracy. In order to gauge the accuracy of the Boussinesq model for longer-term simulations, further comparisons were made between power spectral densities of the free surface and horizontal velocity components computed with the Boussinesq model versus measured time series during the campaign (see supplementary material). These comparisons show that the main features of the spectra matched, and together with the well reproduced average drifter locations, these comparisons build confidence into the model's capability to also simulate larger circulation structures.

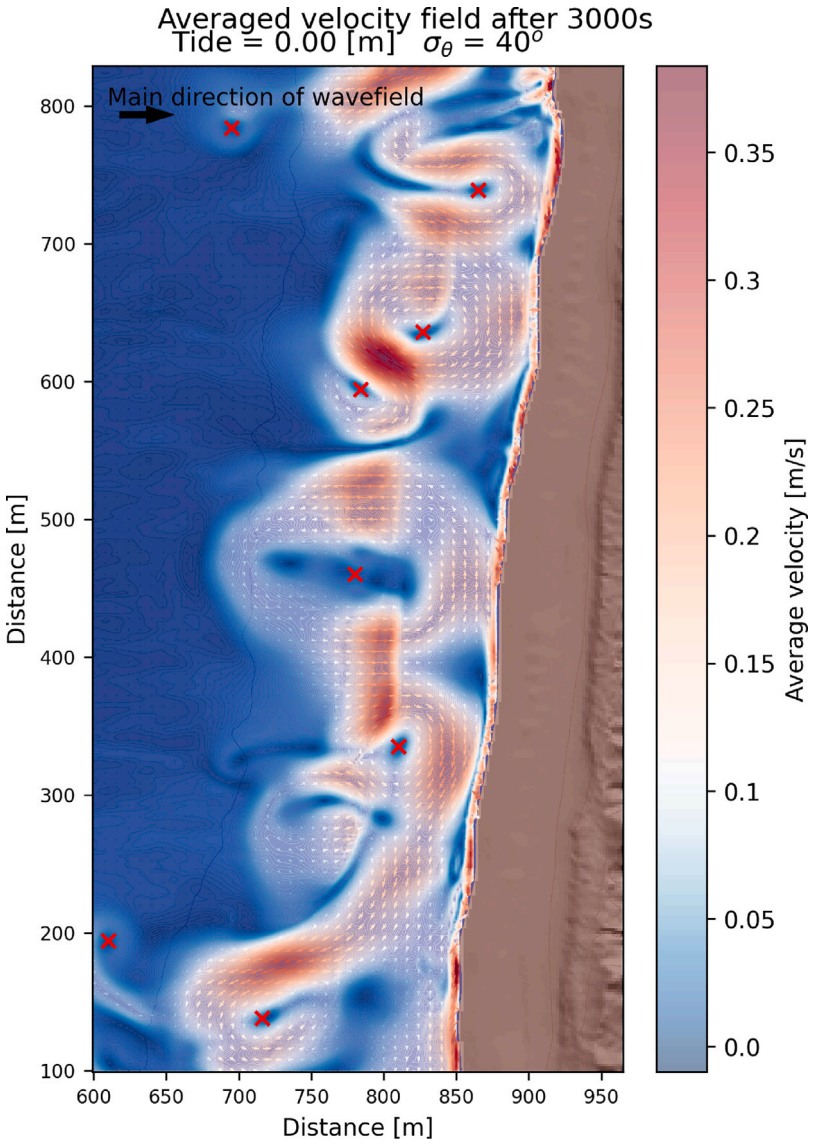

Fig. 6. Average velocity field for one simulation with multiple eddies of different size and strength. The red crosses denote where centers of these eddies were identified. Input parameters are tide= 0 m, $\sigma_\theta = 40°$ and $D_p = 0°$.

4. Circulation patterns

We now proceed to the numerical study of nearshore circulation and the dependence on wave and tidal conditions. Simulations are run with an array of input parameters using the bathymetry from Sylt detailed in the last section. It will come to light that depending on the wave and tide parameters, the nearshore currents come in various different forms. We will compare the dependencies against the work of Spydell and Feddersen (2009), Baker et al. (2021), Choi et al. (2015), and O'Dea et al. (2021), and also look at a larger scale comparison with the results of Scott et al. (2014).

4.1. Model input

The model was run with various values of three main parameters: the tide level; the directional spread σ_θ, and main direction D_P of the incoming wave field. Browsing through the Bunker Hill buoy records, realistic values of the latter two variables are found to be σ_θ between 0 and 40°, and the peak direction D_P between 270 and 310°. Further from using the OSU Tidal Prediction Software (OSU Tidal Prediction Software, 2020) we found that the tide naturally varies between −0.5 m and 0.5 m. We discretized these parameters as follows:

Tide level: $-0.5, -0.25, 0, 0.25, 0.50$ m,
Directional spread: $\sigma_\theta = 0, 20, 40°$,
Peak direction: $D_P = 270, 290, 310°$.

Altogether this yields 45 different simulations. The tide is modeled as a stationary change to the water depth, i.e. a mean tidal level constant during a 60 min run. Throughout, the sea state is defined by $H_s = 0.75$ m and $T_p = 9.1$ s which corresponds to the conditions during the field campaign. To generate the JONSWAP spectrum the wavemaker technique of Wei et al. (1999) is used. The directional spreading was again modeled with the cosine squared assumption as described in Appendix B. To generate the binning a spectral frequency resolution of $\Delta f = 1/3600$ s^{-1} to avoid wave maker recurrence during the run, which resulted in 1099 distinct frequencies bins between 0.036–0.341 Hz. Similarly, the directional bins had a resolution of 1° resulting in $1, 41, 81$ directional bins for the three different directional spreads.

While the bathymetry is considered to be static, a changing tide level impacts the depth of features on the seafloor and therefore impacts the overall flow. Thus in a certain sense the changing tide level can be interpreted as a change in bathymetry. Further, wavefields

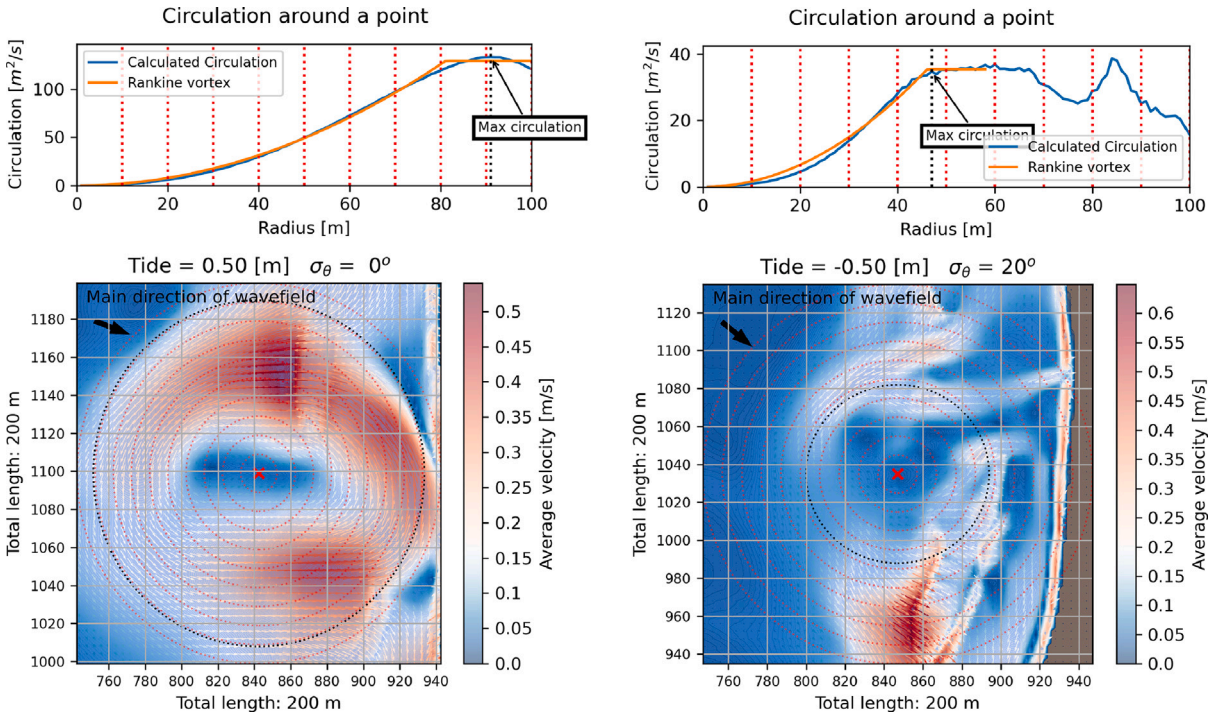

Fig. 7. Inspection of the circulation around two eddies. Top panels show the computed circulation around the identified center for various radii. The dotted red lines denote the radius at intervals of 10 m, and the black dotted line indicates the maximum circulation. Bottom panels show the corresponding velocity field.

approaching the beach at an angle have the potential to create large longshore velocities, while having a higher directional spread allows for the waves to come in from multiple directions creating a more variable incoming field. The objective of this discretization is to see the impact of plausible variations in the input spectrum on the wave regime at the particular location on Sylt. In addition, the bathymetry is the same as described in Section 3, except that we now use the entire 1000 m × 2000 m domain from the measurements. We also now use a standard JONSWAP spectrum, which is the commonly used empirical spectrum for the North Sea area and well representative for the study site.

4.2. Circulation

Each Simulation is run for 3600 s, where the first 600 s are purely for initializing the wave field. After this initial period the ocean surface velocity is continuously averaged. This procedure yields mean values for the velocity which we visually inspect (see Fig. 6) and use for the construction of average streamlines similar to the pathlines observed by Scott et al. (2014). To find the locations of the circulation centers, a review of the data is performed by a two-step method. First, the resulting flow is plotted as in Fig. 6 with the color representing velocity (similar to plotting the swirling strength as defined for example in Buckley and Veron (2017)). This first step marks every location with a circular velocity as a potential center.

After visually inspecting all the images like Fig. 6, the circulation is calculated for every potential vortex by numerically integrating the velocity fields in circular paths for varying radii around the center. Then the maximum circulation is identified by a simple forward difference, which is manually inspected and corrected if necessary. Using this second step, a finer vortex identification criterion is used to determine whether the rough locations indicated in the first step were indeed a center. To count as a vortex the flow needs to fulfill the following criteria:

- The center of the vortex is identified as a region of zero flow since near the center of revolution the computed vortex flow behaves like a solid-body rotation (Kundu and Cohen, 2008).
- The velocity field resembles a closed circuit.
- The circulation must exhibit a local maximum which is used to demarcate the edge of the vortex.

The maximum circulation and the corresponding radius are stored together with the coordinates of the center for further statistical analysis (see Fig. 7 for example).

4.2.1. Visual comparisons

Visual inspection of the velocity fields suggests a striking resemblance to the work of Scott et al. (2014) who found that there exist three primary behavioral groups of the large scale velocity patterns. These three groups are characterized as (a) *exit*, (b) *rotation*, and (c) *longshore*. In our simulations we also found all three groups of behavior, but in the case of flows with strong exit behavior, we also found strong cross-shore flow, so we term the first behavioral group (a) *exit and entry*. All possibilities are shown in Fig. 8.

Further it was found in Scott et al. (2014) that while the behavioral groups identified above are the dominant groups in the short term, some of the drifters used in the underlying data collection campaign followed a composite path. For example a drifter may initially follow a circular path, completing several revolutions around some vortex, before getting dragged into an exit flow and be sent out further offshore. Another scenario observed by Scott et al. (2014) was that drifters were caught in a longshore current, moving up or down the beach. Analyzing the drifter behavior, Scott et al. (2014) deduced that (1) Exit flows feature vortices, spun off from the main flow, similar to separation vortices in high-Reynolds-number viscous flow. (2) Dominant longshore flow often features smaller exit flows along the length of the main flow. (3) Inside longshore flow there exist rotations which the longshore flow swirls around. All of these phenomena appear in our data set as well, indicating that the resulting flow from our inputs to BOSZ and the resulting output reflects real possibilities of nearshore flow.

Examining the first row of Fig. 8 also exemplifies the influence of the ratio of incoming significant waveheight to the local water depth. Indeed, Scott et al. (2014) noted in their field experiments that this ratio is a major factor influencing which of the three primary behavioral

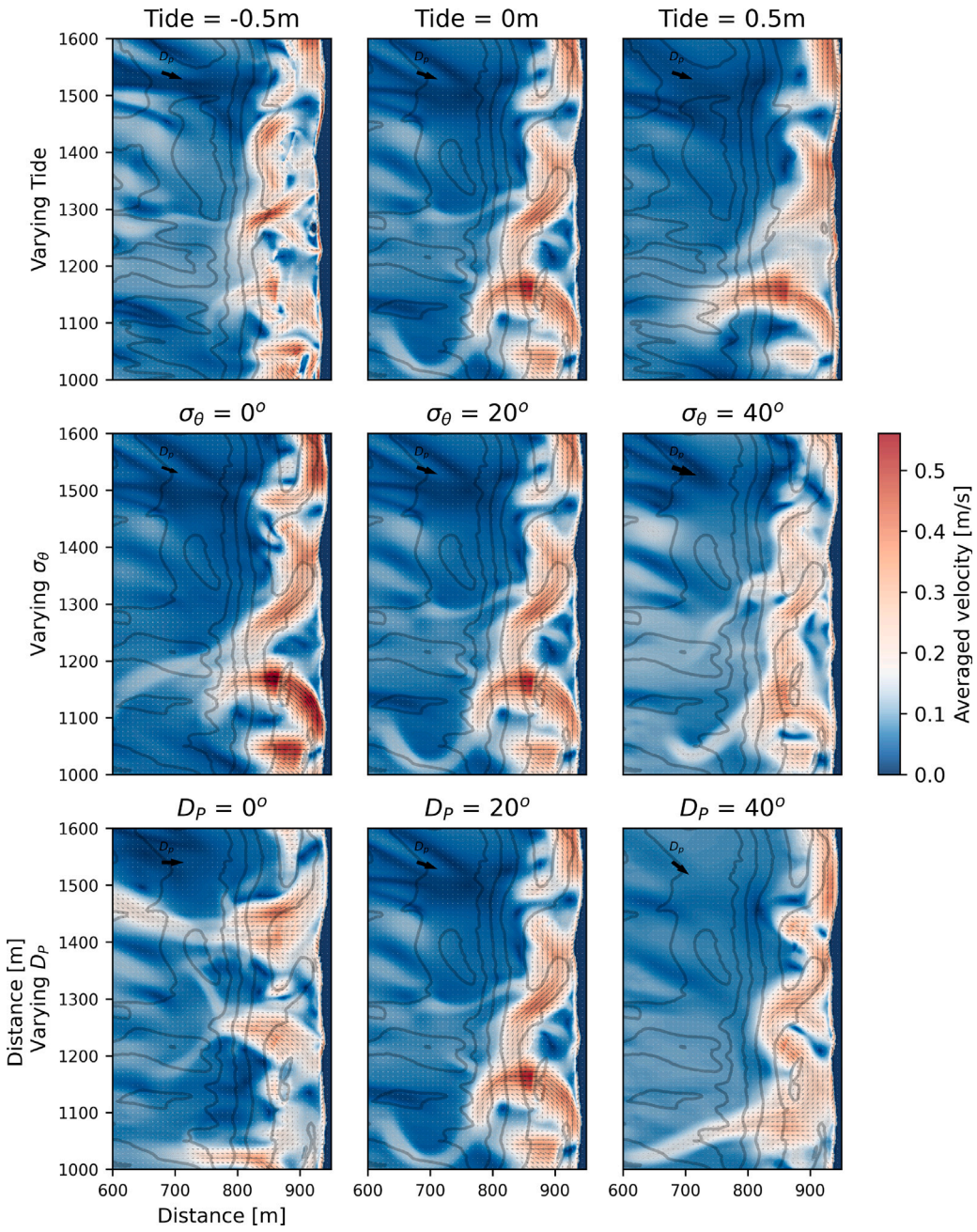

Fig. 8. Qualitative study of dependence of the flow pattern on the input parameters. The upper row shows the average velocity field for directional spread $\sigma_\theta = 20°$, peak direction $D_P = 20°$ and varying tide levels. The middle row shows the average velocity field for tidal level 0, peak direction $D_P = 20°$ and varying directional spreads. The lower row shows the average velocity field for directional spread $\sigma_\theta = 20°$, tidal level 0, and varying peak direction. The peak direction is indicated by the black arrow in the upper left corner of each panel, and the directional spread is indicated by the width of the arrow. The bathymethry is contoured for every meter.

groups mentioned above is prevalent nearshore. Group (b) should be most common when the tide, and thus water depth, was near the seasonal average for the location. Indeed, at tide levels around 0, the sandbar depth is optimal for this kind of flow while both higher and lower tides cause fewer eddies. While we do not vary the significant waveheight in our experiment, the ratio is changing due to different tidal levels, and our results show that for medium values of the tidal level, the largest number of eddies appear. Breaking in the surf zone can cause higher values of flow velocity (Martins et al., 2022), which in turn allows the possibility of flow circulating in larger scale patterns with higher values. This effect might be what causes the size of the eddies to increase for increasing tide, as the breaking locations move further towards the shore and thus towards our area of interest.

Plotting some of the averaged velocity fields for different directional spreads yields the middle row of Fig. 8. As already pointed out in Spydell and Feddersen (2009) and O'Dea et al. (2021), it can also be seen here that lower directional spread is associated with larger velocities in the surf zone, and higher spread yields more and higher variability in the transient flow. Choi et al. (2015) note that the decrease in longshore flow is a consequence of multidirectional phase interaction in the nearshore region, and yields less wave-induced momentum flux based on the moments of the wave energy spectrum. As noted in both Baker et al. (2021) and O'Dea et al. (2021) this does not lower the energy associated with the wave field nearshore, but the resulting wavefields feature greater short-scale fluctuations of the horizontal velocity field which on average leads to more cancellations. Lastly, the main direction of the incoming wave field greatly influences

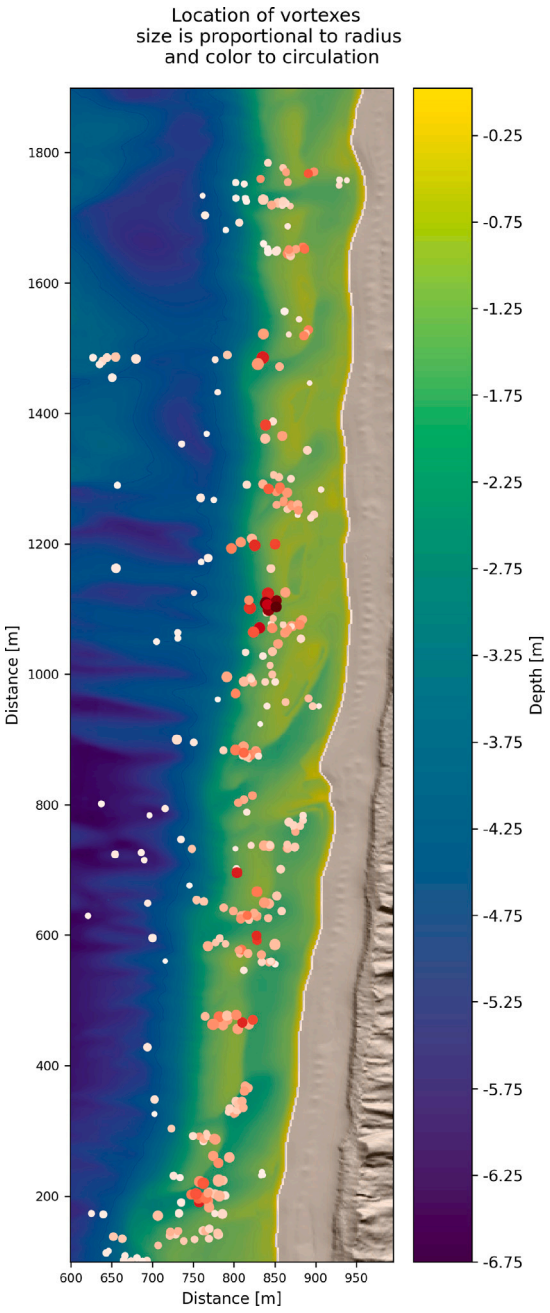

Fig. 9. The location of vortices across all the simulations. Size of circle is proportional to radius, and color indicates strength of circulation. Note that some locations are preferred, such as around the sandbar and at the bottom and mid-point of the picture.

the longshore flow. Indeed, it can be observed in the lower panels of Fig. 8 that with increasing angle between D_P and the normal to the beach, the longshore component of the surf zone currents increases.

It is also evident that most of the vortices appear inside the surf zone as seen on the right side of Fig. 9. All of the vortices found outside the surf zone are due to exit flows which can extend to up to two surf zone widths beyond the surf zone edge, and as noted by Scott et al. (2014), vortices appear around these rip currents. The water depth is also critical for the formation of vortices since wide and strong vortices generally appear directly at the sandbar where the wave-induced velocity is highest (Martins et al., 2022) and these vortices are trapped inside the trough (Bühler and Jacobson, 2001).

4.2.2. Approximation by Rankine vortices

In theoretical fluid dynamics it is common to describe vortex motion using Rankine vortices, which is a combination of the solid-body rotation and the irrotational vortex. For the solid-body rotation, the circulation $\Gamma = 2\pi r^2\omega_0$ is increasing quadratically with increasing radius, and the vorticity is $2\omega_0$. For irrotational vortices, the circulation is constant for all radii, given by Γ_{max} (Kundu and Cohen, 2008). A Rankine vortex is defined by two parameters. The parameter σ determines the radial distance at which the vortex characteristics switch from solid-body rotation to irrotational vortex, and the parameter Γ_{max} determines the maximum circulation. The precise formulation of the circulation in a Rankine vortex is given by

$$\Gamma(r) = \begin{cases} \Gamma_{\max} r^2/R^2, & \text{if } r \le R, \\ \Gamma_{\max}, & \text{if } r > R. \end{cases}$$

While horizontal eddies in the surf zone do not always resemble Rankine vortices (especially if the eddy covers a region where the depth changes significantly), it was found that about 91% of all identified eddies are close to circular, with $1-\frac{r_1}{r_2} < 0.24$ where r_1 is the semi-major axis and r_2 the semi-minor axis. Even for largely elliptical eddies, it is still possible to use the Rankine-vortex analogy by averaging properly. For this, we define the circle equivalent radius $r_c = \sqrt{r_1 r_2}$. This defines the extension of the Rankine vortex to ellipses to be:

$$\Gamma(r) = \begin{cases} \Gamma_{\max} r_c^2/R^2, & \text{if } r \le R, \\ \Gamma_{\max}, & \text{if } r > R. \end{cases}$$

For all identified eddies, the best fit for $\Gamma_{\max}$ and σ were found. Two examples are plotted in Fig. 7. Typical of these plots is that close to the center the Rankine vortex gives a good approximation, but close to $r = \sigma$ the true circulation is almost linearly increasing. The irrotational part of the vortex then takes over, until at increasing distance from the center other parts of the flow take a more significant role, and the flow pattern is no longer reminiscent of a Rankine vortex. Again, while the Rankine vortex itself does not perfectly reflect the dynamics in the surf zone, especially as the depth varies significantly over its extent, it is still a good approximation of the nearshore field. In our simulations, the circular definition fit 91% of the identified eddies.

As also described in Scott et al. (2014), eddies exist in the surf zone exist generally alongside entrance, exit, or longshore flows. For example in Fig. 7 the left eddy is part of a longshore current and the right eddy has a longshore current above it which it feeds into before continuing into an entrance below it. In the upper panel of Fig. 7 the circulation spikes again, but this is purely due to the large velocity in the entrance flow and does not meet our criteria for eddy motion.

4.3. Statistical analysis

Using the two-step method outlined above on the velocity fields of the 45 simulations, and marking all the vortices and calculating their radii and circulation such as in the examples detailed in Fig. 7 yields 343 individual vortices across all simulations. Constructing histograms based on these data yields the plots shown in the upper panel of Fig. 10. In the lower panels of Fig. 10, the dependence of vortex size on the three parameters tide level, D_P and σ_θ is indicated. It is evident that the number of vortices is maximal at mid-tide, with almost twice as many vortices present as during high or low tide. The distribution of large and small vortices also changes with changing tides, and an increasing share of large vortices is generally associated with higher tides.

While the overall number of vortices does not seem to depend on the directional spread σ_θ, the distribution of large and small vortices is highly dependent on the value of σ_θ. Indeed, larger directional spread correlates positively with higher number of small vortices while larger vortices more numerous at low directional spread. Lastly D_P is a critical factor for the number of vortices. If an incoming wavefield is normal to the beach, twice as many vortices develop than during an obliquely

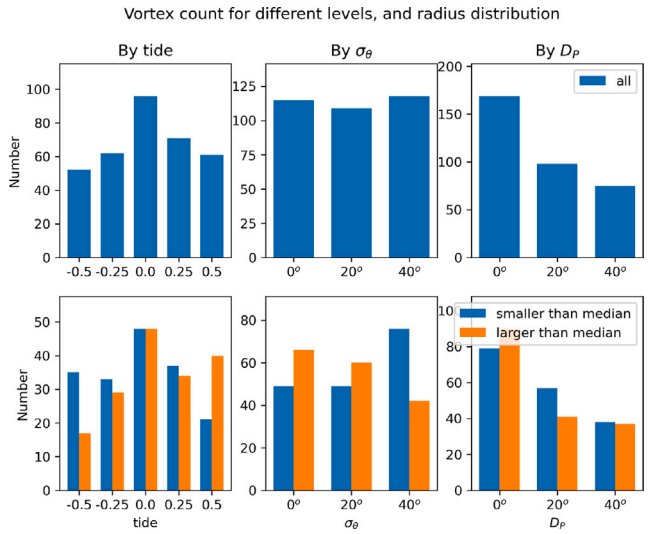

Fig. 10. Upper panels: vortex count as a function of tide level, directional spread σ_θ and peak direction D_P. Lower panels: vortex count by diameter size.

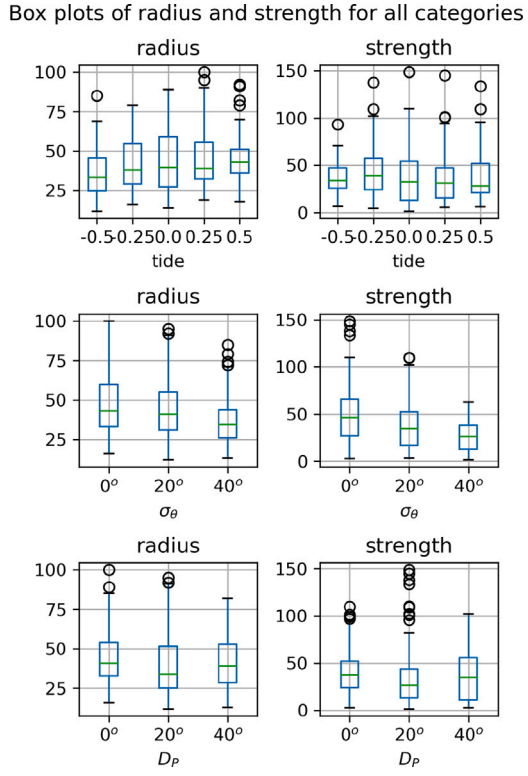

Fig. 11. Box plots of vortex radius and circulation strength containing mean, upper and lower quartiles, maximum value and outliers.

incident wavefield with $D_P = 40°$. Meanwhile, the sizes of the vortices are not clearly correlated with this parameter.

The dependence of the vortex features on the wave and tidal parameters can also be represented in boxplots, such as shown in Fig. 11. Here it can be gleaned that vortex radius and vortex strength are inversely proportional to the directional spread σ_θ (middle panels). In addition, we see that vortex radius is proportional to tidal level such as also observed in less detail in Fig. 10.

While no further clear dependencies can be found in Fig. 11, it is possible to verify the visual identifications and quantify whether any particular combination of the three free parameters has a statistically

Table 1
The table shows p-values from the 3-way ANOVA test for the radius and circulation of vortices. Small p-values correspond to statistically significant influence on the mean, and the most important parameter combinations are shown in bold face.

Dependence	p-values	
	Radius	Strength
Tide	**1.4e−2**	5.6e−2
σ_θ	**1.8e−4**	**3.6e−15**
D_P	5.7e−2	**4.9e−2**
Tide: σ_θ	4.7e−1	3.7e−1
Tide: D_P	3.3e−1	5.2e−1
σ_θ: D_P	2.9e−1	**1.4e−3**
Tide: σ_θ: D_P	9.2e−1	9.9e−1

significant influence of the vortex features. For this, it is necessary to conduct a statistical test, and we are choosing a three-way Analysis of Variance (ANOVA) test. We are interested if any one of the parameters, or a combination of them impacts the mean values of vortex radius and vortex strength to a significant degree. We thus create the 3-way ANOVA model as follows:

$$\text{radius} \sim \text{tide} + \sigma_\theta + D_\theta + \text{tide} : \sigma_\theta + \text{tide} : D_\theta + \sigma_\theta : D_\theta + \text{tide} : \sigma_\theta : D_\theta$$

$$\text{strength} \sim \text{tide} + \sigma_\theta + D_\theta + \text{tide} : \sigma_\theta + \text{tide} : D_\theta + \sigma_\theta : D_\theta + \text{tide} : \sigma_\theta : D_\theta$$

Using the data from Fig. 11 to conduct the 3-way ANOVA test as described above yields the results seen in Table 1. It is evident that the mean radius of the vortices are influenced by the tide, directional spread σ_θ, and main direction D_p and that the mean circulation strength is influenced by the tide, spread σ_θ, main direction D_P and a combination of the latter two.

5. Discussion

Depending on the nature of the incoming wavefield, surf zone dynamics can feature a variety of flow patterns, including longshore currents, entrance and exit flows, rip currents and in many cases eddies of varying size and strength. While it is well known that the bathymetry is the main controlling factor of the nature of the wave-driven nearshore currents (see for example Scott et al. (2014) and McCarroll et al. (2018)), it can also be of value to consider how a combination of wave and bathymetric parameters influences the feature of nearshore flows. For example, Suanda and Feddersen (2015) conducted a model study where the beach slope, significant waveheight, peak period and directional spread are varied. In the present study we have considered the influence of the incident wave field by varying the peak direction and directional spread of the incoming waves. In addition we have varied the tidal level which is similar to, but weaker than bathymetric forcing.

Using an array of 45 different parameter values, each simulated for one hour, we have identified various flow patterns, and focused in particular on identifying eddies in the nearshore zone. Most of the eddies identified in the present study are close to circular which suggests comparison with a Rankine vortex which is a concept often used in theoretical fluid dynamics. Using this construct as a tool can help identify the size and strength of a given eddy.

The main features of the flow as well as details like the size (radius) and strength (circulation) of these vortices can easily be determined. For eddies with large eccentricity, we have used an averaging procedure to still be able to define the radius and circulation strength.

We found that when the tide is at a certain ratio compared to the depth of the sandbar, a large number of organized circulations arises as seen in Fig. 10. When much of the incoming wave energy breaks at the same location the return flow of the waves feeds into energetic and organized motions in the form of eddies but also rip currents. The

local bathymetry is also a controlling factor for the size of the eddies, and the histogram in Fig. 10 shows that the predominant shape of eddy size changes from small to large for increasing tide levels. Additionally, the peak direction of the wavefield is also an important factor for eddy formation. When waves approach the shore at an angle, the longshore velocity can become dominant over the strength of the vortex flow. The intensity of the longshore flow decreases towards its offshore and onshore boundaries (see Fig. 1, right panel) and may also vary in time. Consequently, the net longshore flow prevents the formation of distinct circulatory patterns of smaller scale. Similar dynamics were also observed by Choi et al. (2015). However, when eddies do appear, for example in the wake of an exit flow or the shadow of a swing in the longshore current, then we found evidence that the and strength of these eddies seem to be affected by the peak direction of the wave field but not in a clear manner.

Lastly the directional spread of the incoming waves impacts the distribution of large and small eddies, their strength, and their average size. A possible explanation could be that when waves approach the beach at multiple angles, some destructive interference occurs that reduces the strength of the flow inside the surf zone. When averaging over longer time spans the vorticity decreases for larger directional spreads in the incoming wavefield as also found in Spydell and Feddersen (2009) and O'Dea et al. (2021). Our analysis also shows that with less vorticity on average, it follows that the circulatory strength of the vortices also diminishes for higher directional spreads. In the case of no directional spread from the incoming wavefield (i.e. $\sigma_\theta = 0$), all the vorticity in the surf zone is bathymetry controlled. Since the bathymetry is constant across all computations in the present work, it is natural that the average vorticity and thus circulatory strength is larger for unidirectional waves. This observation also supports the conclusion that bathymetry-driven vorticity is the main force of vortex formation in the surf zone. High directional spread inhibits vortex formation by nonlinear interactions, since inside the surf zone higher spread induces wave breaking along directions that are not aligned with the main flow, thus reducing the speed, at which it flows (see Choi et al. (2015)). This finding also concurs with the results of Baker et al. (2021) who found that on average, smaller radii are connected to higher directional spread.

Overall, it is found that peak direction D_P, the directional spread σ_θ, and the tidal level have a strong influence on the characteristics of the appearing vortices, both in terms of size and strength. As can be seen in Table 1, the directional spread has the largest overall statistical evidence of the influence on the vortex characteristics, and in particular on the resulting vortex strength. On the other hand, the peak direction of the incoming wavefield has the largest influence on number of vortices (see Fig. 10 and on the strength of the longshore flow (see Fig. 8)). In addition we have seen that tidal level and directional spread influence the distribution of large versus small vortices, while the tidal elevation influences the total numbers of vortices. While it is generally understood that the nearshore bathymetry is an important factor in the development of nearshore circulation, future studies should quantify at which tidal level the characteristics of the wave field become more important than the bathymetry itself. Finally, Table 1 reveals the significant *joint* influence of peak direction and directional spread of the wave field for which we have no physical explanation for at this point.

CRediT authorship contribution statement

Andreas Bondehagen: Writing – review & editing, Writing – original draft, Visualization, Validation, Software, Methodology, Investigation, Formal analysis, Data curation, Conceptualization. **Volker Roeber:** Writing – review & editing, Writing – original draft, Visualization, Validation, Supervision, Software, Project administration, Methodology, Investigation, Funding acquisition, Formal analysis, Data curation, Conceptualization. **Henrik Kalisch:** Writing – review & editing, Writing – original draft, Visualization, Validation, Supervision, Software, Project administration, Methodology, Investigation, Funding acquisition, Formal analysis, Data curation, Conceptualization. **Marc P. Buckley:** Visualization, Validation, Software, Resources, Project administration, Methodology, Investigation, Funding acquisition, Formal analysis, Data curation, Conceptualization. **Michael Streßer:** Visualization, Validation, Software, Resources, Methodology, Investigation, Formal analysis, Data curation, Conceptualization. **Marius Cysewski:** Resources, Methodology, Investigation, Formal analysis, Data curation. **Jochen Horstmann:** Writing – review & editing, Supervision, Resources, Project administration, Conceptualization. **Maria Bjørnestad:** Visualization, Validation, Software, Resources, Methodology, Investigation, Formal analysis, Data curation, Conceptualization. **Olufemi E. Ige:** Investigation, Formal analysis. **Hege G. Frøysa:** Resources, Investigation. **Ruben Carrasco-Alvarez:** Resources, Data curation.

Declaration of competing interest

The authors declare that they have no known competing financial interests or personal relationships that could have appeared to influence the work reported in this paper.

Data availability

Wave buoy data and data of acquired and simulated particle trajectories are available for public access at DOI: http://dx.doi.org/10.5281/zenodo.7843727. The BOSZ code is available upon reasonable request.

Acknowledgments

The authors would like to thank Jan Bödewadt and Jurij Stell for technical support, and Lutz Christiansen and the LKN.SH (Landesbetrieb für Küstenschutz, Nationalpark und Meeresschutz Schleswig-Holstein) for providing bathymetric data for the bathymetry around Sylt. The authors would like to thank Christine Baker for helpful conversations and Falk Feddersen and one anonymous reviewer for providing insightful comments that helped improve the quality of the paper significantly.

We acknowledge funding from the Research Council of Norway under grant no. 239033/F20, from the European Union's Horizon Europe research and innovation programme under the Marie Skłodowska-Curie grant agreement No. 101119437, from Bergen Universitetsfond, from the "Changing Earth – Sustaining our Future" program of the Helmholtz Association, and support from the Deutsche Forschungsgemeinschaft, Germany (DFG, German Research Foundation, project number 274762653, Collaborative Research Centre TRR 181 *Energy Transfers in Atmosphere and Ocean*). Volker Roeber acknowledges financial support from the I-SITE program Energy & Environment Solutions (E2S), the Communauté d'Agglomération Pays Basque (CAPB), and the Communauté Région Nouvelle Aquitaine (CRNA) for the chair position HPC-Waves and the support from the European Union's Horizon 2020 research and innovation programme under grant agreement No 883553.

Wave buoy data and data of acquired and simulated drifter trajectories are available for public access at DOI: 10.5281/zenodo.7843727. The BOSZ code is available upon reasonable request.

Appendix A. Camera calibration

A central problem for the verification of the model is the comparison of movement of actual drifters recorded through a stereo camera setup to the simulated Lagrangian drifters described above. To perform this comparison, it is necessary to transform the pixel coordinates of the two cameras to three-dimensional world coordinates. This is done with the same method as described by Bjørnestad et al. (2021), using a linear transformation. The linear transform consists of two matrices: an extrinsic matrix to transform the world coordinates to camera coordinates, and an intrinsic matrix to compensate for lens distortion. This transformation is defined as:

$$\begin{pmatrix} u \\ v \\ 1 \end{pmatrix} = \begin{bmatrix} f_x & s & c_x \\ 0 & f_y & c_y \\ 0 & 0 & 1 \end{bmatrix} \begin{bmatrix} r_{11} & r_{12} & r_{13} & t_1 \\ r_{21} & r_{22} & r_{23} & t_2 \\ r_{31} & r_{32} & r_{33} & t_3 \end{bmatrix} \begin{pmatrix} X \\ Y \\ Z \\ 1 \end{pmatrix}, \tag{1}$$

where (u, v) are the pixel coordinates and (X, Y, Z) are world coordinates. The 3×4-matrix defines the extrinsic coordinates and consists of rotation and translation elements r_{ij} and t_i, respectively which rotate and translate the world coordinates to match the camera's field of view. The 3×3-matrix is the intrinsic matrix which consists of compensation factors f_x and f_y for the focus of the camera which changes how large objects appear. The coefficients c_x and c_y translate the location of the pinhole if it is not in the center of the camera. Lastly, the parameter s compensates for the skewness of camera axes. These parameters might be different for different locations in the cameras view as well, due to imperfections in the camera's construction. It might therefore be necessary to create multiple such transformations for different locations in the field of view. Now to go from pixel coordinates to world coordinates it is necessary to use a stereo camera to determine the third world coordinate. This is done by using geometry and the fact that the two cameras are defined to have the same Y and Z coordinates. Then the Z value of the world point of one pixel is

$$Z = \frac{f_x b}{d},$$

where Z is the coordinate in the "main" camera's coordinate system, f_x is the focal length of this camera, b is the distance between the cameras and d is the disparity of x-coordinates between the two cameras.

In the present work, the built-in MATLAB *Camera Calibration Library* is used to find the transformation matrixes. This toolbox provides functions to calibrate of the stereo cameras (i.e. to find the intrinsic and the extrinsic matrices), and also to triangulate points in the images, meaning to transform from pixel coordinates to world coordinates. By default, MATLAB describes the world points in the following coordinate system centered at the lens of Camera 1. :

X: direction towards camera 2

Y: downwards

Z: orthogonal to X and Y, pointing away from Camera 1 towards FOV.

Hence it is necessary to perform a change of basis. If multiple ground control points inside the pictures have known coordinates in both the cameras coordinates and for example in WGS84, then it is possible to change the coordinates through the transformation

$$P_{C \to WGS84}[x]_c = [x]_{WGS84}.$$

The change of basis matrix $P_{C \to WGS84}$ is the same as described in (Lay, Lay and McDonald, 2016). Thus, if the cameras are calibrated and the pixel locations of drifters are known it is possible to calculate the corresponding location in world coordinates.

After arriving at the Bunker Hill site on Sylt and setting up the cameras, a checkerboard was carried around inside the field of views of the cameras (see Fig. 12). This was done to collect multiple pictures of a known geometry from multiple angles and locations to later calibrate the cameras. By choosing a subset of these images MATLAB can create the matrices for the stereo cameras. About 120 pairs of images were chosen to create the above image shown in Fig. 13, which created a geometry which matched with the known distances of the testing area. Now by finding all the pixel values of a drifter's path, MATLAB can recreate the path in 3D world coordinates. The following days poles with known coordinates were set up, and during high tide oranges were thrown out onto the sea. Here it was now possible to follow the drifter's position on the images using a MATLAB script. By supplying the initial position of the oranges, it follows the locations of the whitest pixel values in the surrounding areas. This means on the other hand that it is difficult to follow the orange through breaking waves since the white-caps complicates locating the oranges in the frame. After tracking an orange, one can use MATLABs inbuilt triangulations function to find the world coordinates of all the pixel points the orange has occupied. But the original coordinate system which MATLAB supplies is not useful for us, hence it is necessary to change it. Followed the lead of Bjørnestad et al. (2021), we are using a coordinate system, where a orthogonal right handed coordinate system which $x-$ and $y-$ basis vectors is parallel to the sea surface is found between the poles. After this it was necessary to rotate these basis vectors around the z-axis to align the $x-$ and y-axis with the North and East basis vectors of WGS84 as described above such that the locations can be plotted together with the bathymetry described in this data.

Appendix B. Reconstructing 2d spectra from 1D spectra

Buoy readings from the directional Waverider buoy "Buoy Bunker-Hill1" located at 8.272° East, 54.792° North in about 10 m water depth.[1] The data include directional information which allows us to reconstruct the two-dimensional spectrum.

Following Pierson et al. (1971), we incorporate the information about peak direction D_P and directional spread σ_θ by stipulating the function

$$D(\theta) = \begin{cases} a\cos^2(k(\theta - D_P)), & D_P - \sigma_\theta\kappa \le \theta \le D_P + \sigma_\theta\kappa, \\ 0, & \text{otherwise}, \end{cases}$$

where D_P denotes the peak direction and σ_θ denotes the directional spread, and κ is a positive factor. To determine the constants a and k, we have to solve the system of equations

$$\int_{D_P-\sigma_\theta\kappa}^{D_P+\sigma_\theta\kappa} a\cos^2(k(\theta - D_P))\, d\theta = 1$$
$$a\cos^2(k\sigma_\theta\kappa) = 0.$$

The solution of this system of equations corresponding to half a period is:

$$a = \frac{\pi}{\sigma_\theta\kappa}, \qquad k = \frac{\pi}{2\sigma_\theta\kappa}$$

Now to use these results together with the input data it is necessary to discretize both the frequency and angle. This is done with the following discretization:

$$f_i = \{f_1, f_2, f_3, \dots, f_n\} \text{ and } \theta_j = \{\triangle\theta, 2\triangle\theta, 3\triangle\theta, \dots, n\triangle\theta\}$$

with $\triangle\theta = 2\pi/n_\theta$.

Then for each f_i, let θ_m be the largest θ_j such that $\theta_j \le D_p - \sigma_\theta\kappa$ and let θ_n be the smallest θ_j such that $\theta_j \ge D_p + \sigma_\theta\kappa$. For every θ_j, where $j \in [m, n]$, the PSD at this index is then evaluated as

$$E(f_i, \theta_j) = \frac{E_{\max}}{\triangle\theta} E_{10}(f_i) D_i(\theta_j),$$

where E_{10} is the power spectral density from the Bunker Hill buoy in 10 m depth, $E_{\max}$ is a scaling factor, and D_i is the directional function for this frequency. Now the only data accounted for is the first four columns, and the relative PSD. It could be possible to include the skewness and kurtosis if one used the normal distribution as a base instead.

[1] http://codm.hzg.de.

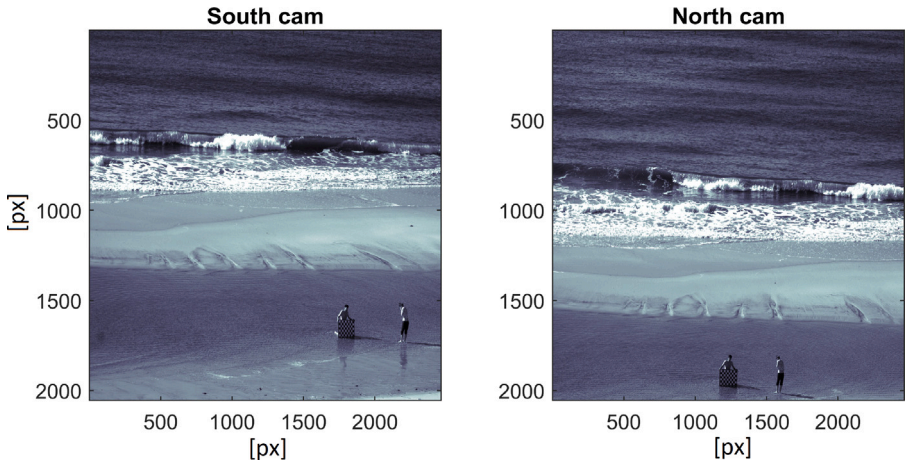

Fig. 12. A checkerboard used for calibrating the cameras was carried around on the beach at low tide. Here seen through both cameras.

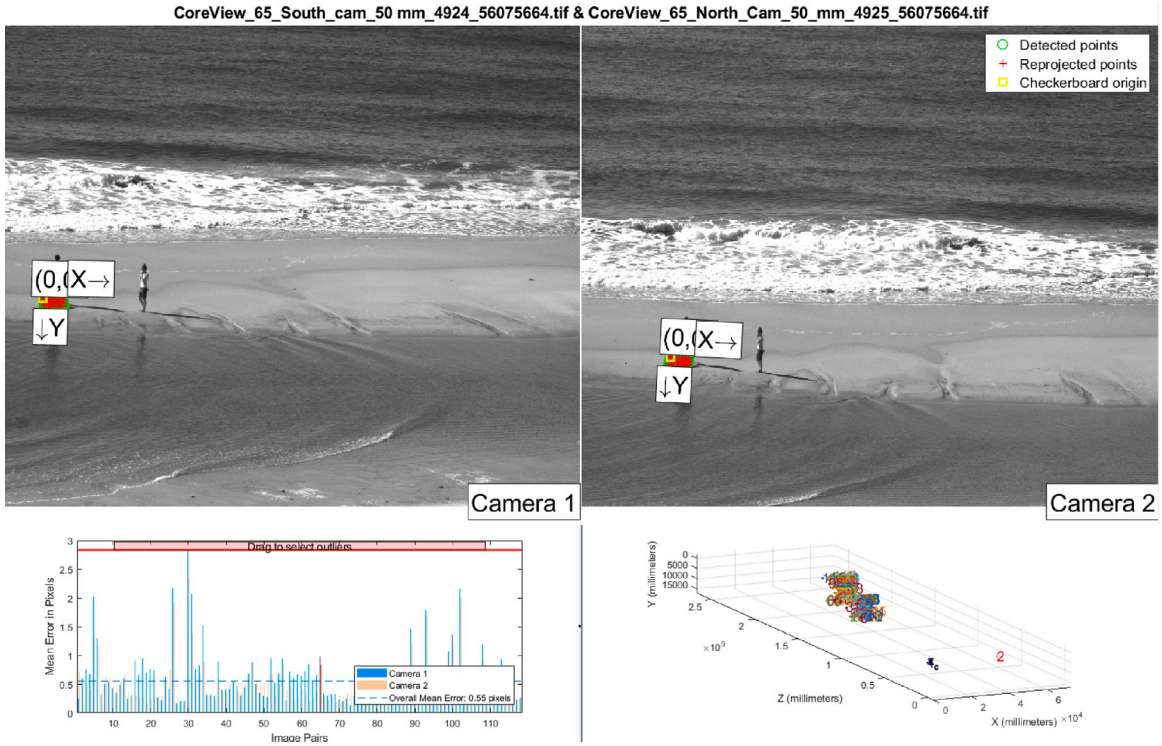

Fig. 13. The calibration software supplied by MATLAB. In the top row is the reprojected checkerboard locations for one image pair. In the bottom left the error of these reprojections is shown for each pair of images and in the bottom right the locations of the checkerboard in the cameras coordinate system is shown.

Appendix C. The BOSZ model

The equations express a balance between flux and dispersion with additional source terms. They can be cast in vector form and are shown here in x-direction only as

$$\mathrm{U}_t + \mathscr{F}(\mathrm{U})_x + \mathscr{G}(\mathrm{U})_y - \mathscr{S}_{bed} = -\mathscr{S}_{dsp} + \mathscr{S}_{frc} + \mathscr{S}_{wbr} + \mathscr{S}_{wmk} \tag{2}$$

where U is the vector of conserved variables, $\mathscr{F}(\mathrm{U})$ and $\mathscr{G}(\mathrm{U})$ is the flux vector, $\mathscr{S}(\mathrm{U})_{bed}$ is the bed slope source term, $\mathscr{S}(\mathrm{U})_{dsp}$ includes the dispersion terms with spatial derivatives, $\mathscr{S}(\mathrm{U})_{frc}$ accounts for bottom friction, $\mathscr{S}(\mathrm{U})_{wbr}$ is a dissipative term to account for breaking waves, and $\mathscr{S}(\mathrm{U})_{wmk}$ represents local wave generation similar to the wave generation method of Wei et al. (1999). Off-shore and lateral boundary conditions are radiation conditions, and outgoing waves are damped with sponge layers (cf. Larsen and Dancy (1983)). The vector functions in (2) are given in differential form as

$$\mathrm{U} = \begin{bmatrix} H \\ P \\ Q \end{bmatrix} \quad \mathscr{F}(\mathrm{U}) = \begin{bmatrix} Hu \\ Hu^2 + \frac{1}{2}g\eta^2 + g\eta h \\ Huv \end{bmatrix} \quad \mathscr{G}(\mathrm{U}) = \begin{bmatrix} Hv \\ Huv \\ Hv^2 + \frac{1}{2}g\eta^2 + g\eta h \end{bmatrix} \tag{3}$$

$$\mathscr{S}(\mathrm{U})_{bed} = \begin{bmatrix} 0 \\ g\eta h_x \\ g\eta h_y \end{bmatrix} \qquad \mathscr{S}(\mathrm{U})_{dsp} = \begin{bmatrix} \psi_C \\ u\psi_C - H_t\psi_P + H\psi_{P2} \\ v\psi_C - H_t\psi_Q + H\psi_{Q2} \end{bmatrix} \tag{4}$$

$$\mathscr{S}(\mathrm{U})_{frc} = \begin{bmatrix} 0 \\ \frac{gn^2u\sqrt{u^2+v^2}}{H^{1/3}} \\ \frac{gn^2v\sqrt{u^2+v^2}}{H^{1/3}} \end{bmatrix} \qquad \mathscr{S}(\mathrm{U})_{wbr} = \begin{bmatrix} 0 \\ 2(\nu_t H u_x)_x + [\nu_t H(u_y^\alpha + v_x^\alpha)]_y \\ 2(\nu_t H v_y)_y + [\nu_t H(u_y^\alpha + v_x^\alpha)]_x \end{bmatrix} \tag{5}$$

$$\mathscr{S}(\mathrm{U})_{wmk} = \begin{bmatrix} \sum_{i=1}^{M_\omega}\sum_{j=1}^{M_\theta} D_{ij}\ \cos\left[\left(k_i sin\theta_j\right) y - \omega_i\ t + \phi_{ij}\right] \\ 0 \\ 0 \end{bmatrix} \tag{6}$$

Here, H and h are the total flow depth and still water depth, respectively. u is the horizontal velocity, g is gravity, η denotes the free surface, n is the Manning roughness coefficient of units $[sm^{-1/3}]$ and ν_t is the eddy viscosity necessary for wave breaking closure. The wavemaker source term generates an oscillating superposition of individual monochromatic waves each with a random phase, ϕ, magnitude D, wave number k, and angular frequency, ω, over the entire computed time, t. The frequency binning is chosen as explained in Roeber et al. (2019) to avoid recycling of the wavemaker input signal.

The local acceleration term in the momentum equation accounting for frequency dispersion with mixed space–time derivatives is given by

$$P = Hu + \frac{z_\alpha^2}{2}\left[Hu_{xx}\right] + z_\alpha\left[H(hu)_{xx}\right] \tag{7}$$

$$Q = Hv + \frac{z_\alpha^2}{2}\left[Hv_{yy}\right] + z_\alpha\left[H(hv)_{yy}\right] \tag{8}$$

and the dispersion terms with only spatial derivatives are denoted by

$$\begin{aligned}\psi_C = &\left[\left(\frac{z_\alpha^2}{2} - \frac{h^2}{6}\right)h(u_{xx} + v_{xy}) + \left(z_\alpha + \frac{h}{2}\right)h((hu)_{xx} + (hv)_{xy})\right]_x \\ &+ \left[\left(\frac{z_\alpha^2}{2} - \frac{h^2}{6}\right)h(u_{xy} + v_{yy}) + \left(z_\alpha + \frac{h}{2}\right)h((hu)_{xy} + (hv)_{yy})\right]_y\end{aligned} \tag{9}$$

$$\psi_P = \frac{z_\alpha^2}{2}u_{xx} + z_\alpha(hu)_{xx} \tag{10}$$

$$\psi_Q = \frac{z_\alpha^2}{2}v_{yy} + z_\alpha(hv)_{yy} \tag{11}$$

and similarly the dispersion terms with time dependent derivatives are denoted by

$$\psi_{P2} = \frac{z_\alpha^2}{2}v_{xyt} + z_\alpha(hv)_{xyt} \tag{12}$$

$$\psi_{Q2} = \frac{z_\alpha^2}{2}u_{xyt} + z_\alpha(hu)_{xyt} \tag{13}$$

where z_α is the reference depth, at which the horizontal velocity is evaluated. The position influences the dispersion properties where values closer to the free surface favor the accuracy of short wave dispersion and vice versa. Since the free surface is the result of a superposition of multiple individual waves, the reference depth has to work for a wide range of wavelengths and cannot be set simply for only one single frequency. A value around mid-depth such as $z_\alpha = -0.531$ h provides optimized shoaling and dispersion properties for a range of waves within $kh < \pi$.

The term $\mathscr{S}(\mathrm{U})_{wbr}$ is the well-known concept of an eddy viscosity extension for the Boussinesq-type equations which is added to the governing equations. This approach diffuses the wave breaking front so that the slope of the free surface cannot develop a sharp shock-front. The diffusion terms in the momentum equations of $\mathscr{S}(\mathrm{U})_{wbr}$ involve the time-varying quantity of eddy viscosity ν_t, which sets the magnitude or strength of the diffusion term. One way to determine the eddy viscosity is by using a one-equation model for the turbulent kinetic energy (TKE), which holds as a proxy for ν_t through the following relation that was introduced by Prandtl et al. (1945) and Kolmogorov (1941) as

$$\nu_t = C_\nu\sqrt{k}l_t, \tag{14}$$

where ℓ_t is the mixing length and taken as the local still water depth in this study. Following Nwogu (1996), we use $C_\nu = 0.55$.

The one-equation closure for k is given by Pope and Pope (2000) as

$$k_t = -\mathscr{A} - \mathscr{E} + \mathscr{P} + \mathscr{D}, \tag{15}$$

where $\mathscr{A}$, $\mathscr{E}$, $\mathscr{P}$, $\mathscr{D}$ denote advection, elimination/destruction, production, and diffusion of TKE, denoted by k.

The terms of Eq. (15) are detailed in Nwogu (1996) and involve several empirical coefficients.

The TKE advection terms is defined as

$$\mathscr{A} = uk_x + vk_y \tag{16}$$

The TKE elimination/destruction terms is based on the work of Launder and Spalding (1974) and is denoted as

$$\mathscr{E} = C_D\frac{k^{3/2}}{\ell_t}, \tag{17}$$

where $C_D = C_\nu^3$.

The TKE diffusion term is small and based on the kinematic viscosity of water, ν. Here we use $\nu = \frac{\mu}{\rho} \approx 0.001$ [m^2/s].

$$\mathscr{D} = \nu(k_{xx} + k_{yy}) \tag{18}$$

The last term is the production of TKE. It is only computed in a cell where a criterion is fulfilled, for example $Fr = \sqrt{\frac{u|_\eta^2 + v|_\eta^2}{gh}} > 0.85$ is exceeded. A parameter B works as a flag and takes on either 0 or 1 depending on the previous inequality. We use the formulation used by Nwogu (1996) with a modification consistent with the fundamental derivation of the production term of TKE as

$$\mathscr{P} = B\frac{l_t^2}{\sqrt{C_d}}\left[u_z|_\eta^2 + v_z|_\eta^2\right]^{\frac{3}{2}} \tag{19}$$

where the flow velocities $u|_\eta$ and $v|_\eta$ are computed at the free surface η. The vertical velocity as well as the vertical gradients of the horizontal velocities can be computed from the truncated Taylor series expansion in combination with the vertical irrotationality condition ($w_x = u_z, w_y = v_z$) at the free surface as

$$\begin{aligned}u_z|_\eta &= -\eta\left[u_{xx} + v_{xy}\right] - \left[(hu)_{xx} + (hv)_{xy}\right] \\ v_z|_\eta &= -\eta\left[u_{xy} + v_{yy}\right] - \left[(hu)_{xy} + (hv)_{yy}\right].\end{aligned} \tag{20}$$

Appendix D. Supplementary data

Supplementary material related to this article can be found online at https://doi.org/10.1016/j.coastaleng.2024.104591.

References

Baker, C.M., Moulton, M., Raubenheimer, B., Elgar, S., Kumar, N., 2021. Modeled three-dimensional currents and eddies on an alongshore-variable barred beach. J. Geophys. Res.: Oceans 126, e2020JC016899.

Bakhoday-Paskyabi, M., 2015. Particle motions beneath irrotational water waves. Ocean Dyn. 65, 1063–1078.

Benetazzo, A., 2006. Measurements of short water waves using stereo matched image sequences. Coast. Eng. 53, 1013–1032.

Bergamasco, F., Torsello, A., Sclavo, M., Barbariol, F., Benetazzo, A., 2017. Wass: An open-source pipeline for 3d stereo reconstruction of ocean waves. Comput. Geosci. 107, 28–36.

Bjørnestad, M., Buckley, M., Kalisch, H., Streßer, M., Horstmann, J., Frøysa, H., Ige, O., Cysewski, M., Carrasco-Alvarez, R., 2021. Lagrangian measurements of orbital velocities in the surf zone. Geophys. Res. Lett. 48, e2021GL095722.

Borluk, H., Kalisch, H., 2012. Particle dynamics in the KdV approximation. Wave Motion 49, 691–709.

Brown, J.A., MacMahan, J.H., Reniers, A.J., Thornton, E.B., 2015. Field observations of surf zone–inner shelf exchange on a rip-channeled beach. J. Phys. Oceanogr. 45, 2339–2355.

Brown, M.G., Smith, K.B., 1991. Ocean stirring and chaotic low-order dynamics. Phys. Fluids A 3, 1186–1192.

Buckley, M.P., Veron, F., 2017. Airflow measurements at a wavy air–water interface using piv and lif. Exp. Fluids 58 (161).

Bühler, O., Jacobson, T.E., 2001. Wave-driven currents and vortex dynamics on barred beaches. J. Fluid Mech. 449, 313–339.

Castelle, B., Scott, T., Brander, R., McCarroll, R., 2016. Rip current types, circulation and hazard. Earth-Sci. Rev. 163, 1–21.

Chen, Q., Kirby, J.T., Dalrymple, R.A., Shi, F., Thornton, E.B., 2003. Boussinesq modeling of longshore currents. J. Geophys. Res.: Oceans 108.

Choi, J., Kirby, J.T., Yoon, S.B., 2015. Boussinesq modeling of longshore currents in the sandyduck experiment under directional random wave conditions. Coast. Eng. 101, 17–34.

Clark, D.B., Feddersen, F., Guza, R., 2011. Modeling surf zone tracer plumes: 2. transport and dispersion. J. Geophys. Res.: Oceans 116.

David, C.G., Hennig, A., Ratter, B.M., Roeber, V., Schlurmann, T., et al., 2021. Considering socio-political framings when analyzing coastal climate change effects can prevent maldevelopment on small islands. Nature Commun. 12, 1–19.

Davidson-Arnott, R., Bauer, B., Houser, C., 2019. Introduction To Coastal Processes and Geomorphology. Cambridge University Press.

de Vries, S., Hill, D., De Schipper, M., Stive, M., 2011. Remote sensing of surf zone waves using stereo imaging. Coast. Eng. 58, 239–250.

emodnet, 2020. European Marine Observation and Data Network. European Commission, URL https://emodnet.ec.europa.eu/en/bathymetry.

Feddersen, F., 2014. The generation of surfzone eddies in a strong alongshore current. J. Phys. Oceanogr. 44, 600–617.

Feddersen, F., Clark, D.B., Guza, R., 2011. Modeling surf zone tracer plumes: 1. waves, mean currents, and low-frequency eddies. J. Geophys. Res.: Oceans 116.

Filipot, J.F., Guimaraes, P., Leckler, F., Hortsmann, J., Carrasco, R., Leroy, E., Fady, N., Accensi, M., Prevosto, M., Duarte, R., et al., 2019. La Jument lighthouse: a real-scale laboratory for the study of giant waves and their loading on marine structures. Phil. Trans. R. Soc. A 377, 20190008.

Gallego, G., Benetazzo, A., Yezzi, A., Fedele, F., 2008. Wave statistics and spectra via a variational wave acquisition stereo system. In: International Conference on Offshore Mechanics and Arctic Engineering. pp. 801–808.

Grimes, D., Feddersen, F., Giddings, S., 2021. Long-distance/time surf-zone tracer evolution affected by inner-shelf tracer retention and recirculation. J. Geophys. Res.: Oceans 126, e2021JC017661.

Hally-Rosendahl, K., Feddersen, F., 2016. Modeling surfzone to inner-shelf tracer exchange. J. Geophys. Res.: Oceans 121, 4007–4025.

Hally-Rosendahl, K., Feddersen, F., Clark, D.B., Guza, R., 2015. Surfzone to inner-shelf exchange estimated from dye tracer balances. J. Geophys. Res.: Oceans 120, 6289–6308.

Horrillo, J., Grilli, S.T., Nicolsky, D., Roeber, V., Zhang, J., 2015. Performance benchmarking tsunami models for NTHMP's inundation mapping activities. Pure Appl. Geophys. 172, 869–884. http://dx.doi.org/10.1007/s00024-014-0891-y.

Inman, D.L., Brush, B.M., 1973. The coastal challenge. Science 181, 20–32.

Kalisch, H., Lagona, F., Roeber, V., 2024. Sudden wave flooding on steep rock shores: a clear but hidden danger. Nat. Hazards 1–21.

Kolmogorov, A.N., 1941. Equations of turbulent motion in an incompressible fluid. Dokl. Akad. Nauk SSSR 299–303.

Kundu, P.K., Cohen, I.M., 2008. Fluid Mechanics: Fourth Edition. Academic Press.

Larsen, B.E., Al-Obaidi, M.A.A., Guler, H.G., Carstensen, S., Goral, K.D., Christensen, E.D., Kerpen, N.B., Schlurmann, T., Fuhrman, D.R., 2023. Experimental investigation on the nearshore transport of buoyant microplastic particles. Mar. Pollut. Bull. 187, 114610.

Larsen, J., Dancy, H., 1983. Open boundaries in short wave simulations — a new approach. Coast. Eng. 7, 285–297. http://dx.doi.org/10.1016/0378-3839(83)90022-4, URL https://www.sciencedirect.com/science/article/pii/0378383983900224.

Launder, B., Spalding, D., 1974. The numerical computation of turbulent flows. Comput. Methods Appl. Mech. Engrg. 3, 269–289. http://dx.doi.org/10.1016/0045-7825(74)90029-2, URL https://www.sciencedirect.com/science/article/pii/0045782574900292.

Li, N., Roeber, V., Yamazaki, Y., Heitmann, T.W., Bai, Y., Cheung, K.F., 2014. Integration of coastal inundation modeling from storm tides to individual waves. Ocean Model. 83, 26–42.

LKN, 2021. High-density airborne lidar sensor ideal for challenging coastal survey of sylt. Hydro Int. URL https://www.hydro-international.com/case-study/high-density-airborne-lidar-sensor-ideal-for-challenging-coastal-survey-of-sylt.

Long, J.W., Özkan-Haller, H.T., 2005. Offshore controls on nearshore rip currents. J. Geophys. Res.: Oceans 110.

Lynett, P.J., Gately, K., Wilson, R., Montoya, L., Arcas, D., Aytore, B., Bai, Y., Bricker, J.D., Castro, M.J., Cheung, K.F., et al., 2017. Inter-model analysis of tsunami-induced coastal currents. Ocean Model. 114, 14–32.

Martins, K., Bertin, X., Mengual, B., Pezerat, M., Lavaud, L., Guérin, T., Zhang, Y.J., 2022. Wave-induced mean currents and setup over barred and steep sandy beaches. Ocean Model. 179, 102110.

McCarroll, R.J., Brander, R.W., Scott, T., Castelle, B., 2018. Bathymetric controls on rotational surfzone currents. J. Geophys. Res.: Earth Surf. 123, 1295–1316.

Morichon, D., Roeber, V., Martin-Medina, M., Bellafont, F., Abadie, S., 2021. Tsunami impact on a detached breakwater: Insights from two numerical models. J. Waterw. Port Coast. Ocean Eng. 147, 05021001.

Nader, J.R., Fleming, A., Macfarlane, G., Penesis, I., Manasseh, R., 2017. Novel experimental modelling of the hydrodynamic interactions of arrays of wave energy converters. Int. J. Mar. Energy 20, 109–124.

Nwogu, O.G., 1996. Numerical prediction of breaking waves and currents with a boussinesq model. Coast. Eng. Proc..

O'Dea, A., Kumar, N., Haller, M.C., 2021. Simulations of the surf zone eddy field and cross-shore exchange on a nonidealized bathymetry. J. Geophys. Res.: Oceans 126, e2020JC016619.

OSU Tidal Prediction Software, 2020. Oregon state university. URL https://www.tpxo.net/otps.

Pierson, Jr., W.J., Neumann, G., James, R.W., 1971. Practical Methods for Observing and Forecasting Ocean Waves By Means of Wave Spectra and Statistics. Technical Report, Naval Oceanographic Office NSTL Station MS.

Pinault, J., Morichon, D., Roeber, V., 2020. Estimation of irregular wave runup on intermediate and reflective beaches using a phase-resolving numerical model. J. Mar. Sci. Eng. 8 (993).

Pope, S.B., Pope, S.B., 2000. Turbulent Flows. Cambridge University Press.

Prandtl, L., et al., 1945. Uber ein neues formelsystem fur die ausgebildete turbulenz. Nacr. Akad. Wiss. Gottingen Math-Phys. Kl 6–19.

Putrevu, U., Svendsen, I.A., 1999. Three-dimensional dispersion of momentum in wave-induced nearshore currents. Eur. J. Mech. B Fluids 18, 409–427.

Rilov, G., Dudas, S.E., Menge, B.A., Grantham, B.A., Lubchenco, J., Schiel, D.R., 2008. The surf zone: a semi-permeable barrier to onshore recruitment of invertebrate larvae? J. Exp. Mar. Biol. Ecol. 361, 59–74.

Roberts, J.D., Jones, C., Magalen, J., 2014. Wave Energy Converter (WEC) Array Effects on Wave Current and Sediment Circulation: Monterey Bay CA. Technical Report, Sandia National Lab.(SNL-NM), Albuquerque, NM (United States).

Roeber, V., Bricker, J.D., 2015. Destructive tsunami-like wave generated by surf beat over a coral reef during Typhoon Haiyan. Nature Commun. 6, URL http://dx.doi.org/10.1038/ncomms8854.

Roeber, V., Cheung, K.F., 2012a. BOSZ (Boussinesq ocean and surf zone model). In: Proceedings and Results of the 2011 NTHMP Model Benchmarking Workshop. NOAA Special Report, pp. 1–437.

Roeber, V., Cheung, K.F., 2012b. Boussinesq-type model for energetic breaking waves in fringing reef environments. Coast. Eng. 70, 1–20.

Roeber, V., Cheung, K.F., Kobayashi, M.H., 2010. Shock-capturing boussinesq-type model for nearshore wave processes. Coast. Eng. 57, 407–423.

Roeber, V., Pinault, J., Morichon, D., Abadie, S., Azouri, A., Guiles, M., Luther, D., Delpey, M., Danglade, N., 2019. Improving wave run-up forecasts–benefits from phase-resolving models. Coast. Struct. 2019, 752–761.

Santamaria, F., Boffetta, G., Afonso, M.M., Mazzino, A., Onorato, M., Pugliese, D., 2013. Stokes drift for inertial particles transported by water waves. Europhys. Lett. 102 (14003).

Scott, T., Masselink, G., Austin, M.J., Russell, P., 2014. Controls on macrotidal rip current circulation and hazard. Geomorphology 214, 198–215.

Shanks, A.L., Morgan, S.G., MacMahan, J., Reniers, A.J., 2010. Surf zone physical and morphological regime as determinants of temporal and spatial variation in larval recruitment. J. Exp. Mar. Biol. Ecol. 392, 140–150.

Sharifi, M., Rafiee, S., Keyhani, A., Jafari, A., Mobli, H., Rajabipour, A., Akram, A., 2007. Some physical properties of orange [var. tompson]. Int. Agrophys. 21, 391–397.

Spydell, M., Feddersen, F., 2009. Lagrangian drifter dispersion in the surf zone: Directionally spread, normally incident waves. J. Phys. Oceanogr. 39, 809–830.

Spydell, M.S., Feddersen, F., Guza, R., 2009. Observations of drifter dispersion in the surfzone: The effect of sheared alongshore currents. J. Geophys. Res.: Oceans 114.

Spydell, M., Feddersen, F., Guza, R., Schmidt, W., 2007. Observing surf-zone dispersion with drifters. J. Phys. Oceanogr. 37, 2920–2939.

Suanda, S.H., Feddersen, F., 2015. A self-similar scaling for cross-shelf exchange driven by transient rip currents. Geophys. Res. Lett. 42, 5427–5434.

Svendsen, I.A., 2006. Introduction To Nearshore Hydrodynamics. Vol. 24, World Scientific.

Varing, A., Filipot, J.F., Delpey, M., Guitton, G., Collard, F., Platzer, P., Roeber, V., Morichon, D., 2020. Spatial distribution of wave energy over complex coastal bathymetries: development of methodologies for comparing modeled wave fields with satellite observations. Coast. Eng. 103793.

Varing, A., Filipot, J.F., Grilli, S., Duarte, R., Roeber, V., Yates, M., 2021. A new definition of the kinematic breaking onset criterion validated with solitary and quasi-regular waves in shallow water. Coast. Eng. 164, 103755.

Watanabe, M., Goto, K., Roeber, V., Imamura, F., 2021. Identification of coastal sand deposits from tsunamis and storm waves based on numerical computations. J. Geophys. Res.: Earth Surf. 126, 1–20.

Wei, G., Kirby, J.T., Sinha, A., 1999. Generation of waves in Boussinesq models using a source function method. Coast. Eng. 36, 271–299.